

1 **Analysis of Concurrent Backscatter Coefficients from *In-situ* Cloud**

2 **Probes and Airborne Lidar**

3 **Shawn W. Wagner**

4 *University of North Dakota, Department of Atmospheric Sciences*

5 *Grand Forks, North Dakota, United States*

6 **David J. Delene**

7 *University of North Dakota, Department of Atmospheric Sciences*

8 *Grand Forks, North Dakota, United States*

9 **Abstract**

10 Jet engine power loss due to ice particle accumulation is a recognized aviation hazard.
11 High-altitude cirrus clouds can have ice particle concentrations high enough to be
12 dangerous; therefore, pilots need to be informed when aircraft enter such environments.
13 One approach to determining ice particle concentration is an onboard lidar system. A lidar
14 does not directly measure ice particle concentrations but uses the measured backscatter
15 coefficient. Concurrent lidar measurements are compared to backscatter coefficients
16 derived from the particle size distribution. Particle measurements are obtained from
17 wing-mounted, *in-situ* probes during four sixty-second flight segments at different
18 temperatures (+7°C, +4°C, -33°C, -46°C). The backscatter coefficients derived from
19 external cloud probes (ECP) are correlated (R^2 of 0.9) with measurements by an airborne
20 lidar system known as the Optical Ice Detector (OID). Differences between the
21 backscatter coefficients range from less than one, to more than three standard deviations
22 of the combined OID and ECP uncertainties. The OID and ECP backscatter coefficients
23 are primarily in agreement for three of the four cases, with disagreement for the -33°C
24 case. The ECP derived backscatter coefficients are lower than the OID for three of the
25 cases, with +7°C being the exception. Measurements over four research flights indicate
26 that the total water content is correlated (R^2 of 0.74) with the OID backscatter coefficient.
27 The strong correlation indicates that the OID is a useful instrument for determining ice
28 particle concentrations over a broad range of environments, including at ice water
29 contents as low as 0.02 g per m³.

30 **Significance Statement**

31 The purpose is to evaluate an airborne lidar system's ability to make observations in
32 clouds using research aircraft measurements of Florida thunderstorms. Development of
33 such a system is important for warning flight crews of potentially dangerous conditions.
34 Our results indicate that the lidar system is useful for the detection of such dangerous
35 environments and is a positive step toward improved aircraft passenger safety. Future
36 work should include a wider range of environmental conditions, with more advanced
37 analysis to account for clouds with both liquid water and ice particles.

31 **1. Introduction**

32 Airborne ice particle ingestion into the engines of high-altitude jets can become a
33 serious aviation hazard in certain conditions. A number of power loss events caused by
34 ice ingestion have occurred since 1990 (Lawson *et al.* 1998), which prompted revised
35 regulations of acceptable flight conditions in glaciated clouds. New regulations have
36 created the need for instruments to alert flight crews whenever aircraft enter clouds with
37 ice particle concentrations that pose a threat. The Optical Ice Detector (OID) is an
38 onboard, short-range cloud lidar designed to detect and characterize hazardous cloud
39 environments (Ray *et al.* 2009; Halama *et al.* 2010; Ray and Anderson 2015). As with
40 any cloud lidar, the OID measures backscatter from liquid droplets and ice crystals. The
41 objective of this study is to evaluate OID measurements of unattenuated backscatter using
42 backscatter coefficients derived from particle size distributions obtained from state-of-
43 the-art cloud probe observations. The evaluation uses backscatter coefficient uncertainty
44 obtained by summing the uncertainty in each spectrum size channel. Each channel's
45 uncertainty is obtained by using both particle concentration and the channel width.
46 Quantitative comparisons of OID backscatter to research grade cloud probes is a major
47 step in the deployment of an onboard lidar system to alert flight crews of dangerous ice
48 concentration conditions.

49 Since the early 1990s, there have been over 240 ice ingestion-related incidents
50 involving commuter and large transport aircraft (Mason *et al.* 2006). Many of these
51 aircraft incidents occurred at altitudes greater than 3000 m above MSL (mean sea level)
52 (Bravin *et al.* 2015) and near convective clouds (Haggerty *et al.* 2018). Before the early

53 2000s, the ice particles in convective clouds were believed not to be a threat since they
54 would not adhere to cold aircraft components. However, power loss incident frequency
55 continued to increase as the number of high altitude flights increased. Analysis of 46
56 power loss events above 3000 m MSL indicated that aircraft would gradually lose power,
57 with some aircraft experiencing total engine shut down. Once the aircraft descended to
58 below 3000 m MSL, failed engines were restarted and normal engine performance was
59 restored.

60 In 2002, a transport aircraft with dual ice detectors experienced engine power loss
61 without the presence of supercooled liquid water (Mason *et al.* 2006). Post event analysis
62 concluded that ice ingestion-related shutdowns can take place in environments consisting
63 entirely of ice crystals, not simply in environments with super-cooled liquid water. This
64 aircraft hazard due to ice particles causing engine power loss was termed “ice particle
65 icing” (Mason *et al.* 2006) or “ice crystal icing” (Haggerty *et al.* 2018) to differentiate it
66 from “icing” of surfaces from the impaction of super-cooled liquid droplets. A 2013 event
67 that occurred above 10 km caused permanent damage to engine compressors and
68 prompted an Airworthiness Directive issuance (Airworthiness Directives 2013) on 27
69 November 2013. The Directive required specific Boeing aircraft (models 747-8, 747-8f,
70 and 787-8) to avoid any high ice concentration operations and advise flight crews of
71 potentially dangerous ice particle icing conditions.

72 Cirrus clouds have been shown to contain potentially high ice crystal concentrations
73 that can be harmful to aircraft engine performance (Gayet *et al.* 2012; Heymsfield 1986).
74 Lawson *et al.* 2006a analysis of 22 mid-latitude cirrus clouds had an average ice particle

75 concentration of 1 cm^{-3} , with some concentrations above 5 cm^{-3} . However, most cirrus
76 clouds have concentrations from 0.01 cm^{-3} to 1 cm^{-3} (Krämer *et al.* 2009). Ice crystal
77 concentration increases with higher updraft speed and the subsequent increase in
78 supersaturation (Heymsfield and Miloshevich 1993). Frey *et al.* 2011 found that outflow
79 from developing mesoscale convective systems in Africa contained ice particle
80 concentrations as high as 8.3 cm^{-3} , with subvisible cirrus having an average ice particle
81 concentration of 0.01 cm^{-3} . See Heymsfield *et al.* 2017 for details on cirrus cloud
82 development and properties.

83 Due to their potentially high concentrations, and often lack of visibility to pilots,
84 cirrus clouds pose a large risk for aircraft engine power loss. Mitigating this flight risk
85 requires alerting flight crews of dangerous ice particle concentrations using onboard
86 instrumentation. Research grade instruments for measuring ice particle concentration
87 have been available since the 1970s (Baumgardner *et al.* 2017). Optical array probes are a
88 class of *in-situ* instruments that measure individual particle size using the blockage of
89 light (shadows) on an array of diodes (Fig. 1). The size of all observed particles are
90 binned into channels and combined over a time interval to obtain the particle size
91 spectrum. Optical array probes are attached to aircraft wings via a canister (Fig. 1) that is
92 attached to pylons (Fig. 2) to obtain *in-situ* measurements while passing through clouds.
93 Direct contact of ice particles with probe arms (Fig. 1) can produce particle shattering
94 which corrupts the particle size spectrum measurement. Particle shattering is mitigated
95 using heated anti-shattering tips (Korolev and Isaac 2005). *In-situ* probes and pylons can
96 affect particles within the observation volume, which may alter measurements by

97 reorganization of particle location by size (known as size sorting) and by rotation of ice
98 crystal (Baumgardner 1984).

99 To avoid placing instruments directly into the air stream, instruments have been
100 developed that use flush-mounted windows which allow observations without altering the
101 air flow around an aircraft. One such system is the Backscatter Cloud Probe (BCP),
102 which measures the backwards scattering of a continuous wave laser beam from cloud
103 water droplets and ice crystals (Beswick *et al.* 2014). The BCP has a sample volume of
104 approximately $125 \text{ cm}^3 \text{ s}^{-1}$ (at an aircraft speed of 100 m s^{-1}) that is located approximately
105 4 cm from the aircraft skin. The BCP can measure particle size distributions from a
106 commercial aircraft platform (Beswick *et al.* 2015). BCP measurements were validated
107 by comparing results to those of a Cloud Droplet Probe (CDP) and a Cloud and Aerosol
108 Spectrometer (CAS) probe.

109 **2. Measurements**

110 The OID is similar to the BCP in using an observation window; however, the OID
111 uses a lidar with a conical sample volume that extends up to 10 m from the aircraft (Ray
112 and Anderson 2015). The OID sample volume is $4500 \text{ cm}^3 \text{ s}^{-1}$ at 100 m s^{-1} with a viewing
113 direction perpendicular to the forward motion of the aircraft (Fig. 2). The BCP uses a
114 single linearly polarized wavelength of 658 nm, while the OID uses two wavelengths: a
115 circularly polarized wavelength of 905 nm and a randomly orientated, linearly polarized
116 wavelength of 1550 nm. The circular polarization of the 905 nm beam enables
117 measurement of the fourth Stokes parameter (*V*) (Liou and Yang 2016; Hulst 1981).
118 Backscatter from the 1550 nm wavelength channel of the OID is not used in this study.

119 The OID has been deployed on the North Dakota Cessna Citation Research Aircraft
120 (Delene *et al.* 2019) during several field projects, including a 2015 field project
121 (CAPE2015) to study Florida thunderstorms (Schmidt *et al.* 2019). The Citation Research
122 Aircraft has conducted several research projects to collect cloud microphysical
123 observations using various instrumentation configurations (Skofronick-Jackson *et al.*
124 2014; Jensen *et al.* 2015; Delene 2016). Multiple field projects have included OID
125 measurements; however, this study analyzes data (Wagner and Delene 2020a) only from
126 CAPE2015 flights, which focused on measurements of cirrus cloud anvils from
127 convective storms. An OID is mounted in the Citation Research Aircraft’s fuselage to
128 measure backscattered light from cloud particles slightly ahead of and along the span of
129 the aircraft wing (Fig. 2). A port is fitted with an anti-reflection coated optical window. A
130 fan moves cabin air across the window to prevent water and ice condensation on the
131 inside surface. A detailed OID diagram of the design of the OID appears in Fig. 1 of Ray
132 and Anderson 2015.

133 The OID measurement of backscatter coefficient (β in units of $\text{km}^{-1} \text{ster}^{-1}$) assumes a
134 homogeneous cloud particle distribution over the sampling distance R . The backscatter
135 coefficient is calculated by inverting the returned lidar power $P_{(R)}$ equation,

$$P_R = \beta G_R e^{-2\epsilon R}, \quad (1)$$

136 where $G_{(R)}$ is a light collection efficiency as a function of particle range, ϵ is the extinction
137 coefficient, and R is the range to the particles (Ray and Anderson 2015). The OID emits
138 light pulses at a repetition rate of 20 kHz, with each pulse having a temporal width of 4
139 ns full width at half maximum (Halama *et al.* 2010). The 20 kHz measurements are
140 aggregated to produce 5 Hz raw data. Raw data is averaged to match the 1 Hz external

141 cloud probe (ECP) processed data. While the OID transmits both 905 nm and 1550 nm
142 laser light, absorption at 905 nm by water is approximately one thousand times less than
143 that at 1550 nm. Hence, using only the 905 nm wavelength simplifies analysis by
144 eliminating the consideration of absorption. While a complete OID error analysis is not
145 yet available, the primary error source is likely the inversion of the range-resolved lidar
146 signal to estimate extinction. For additional details regarding lidar retrievals, see Lolli *et*
147 *al.* 2013.

148 The North Dakota Citation Research Aircraft instruments measures atmospheric state
149 parameters such as temperature, relative humidity, and wind velocities, as well as the
150 cloud size distribution using a set of *in-situ* cloud probes. *In-situ* cloud microphysical
151 instrumentation (Fig. 2) includes a Two-Dimensional Stereo (2D-S) probe (Lawson *et al.*
152 2006b), a High-Volume Precipitation Spectrometer Version Three (HVPS3) probe
153 (Kumjian *et al.* 2016), and a Nevzorov probe (Korolev *et al.* 2013a). Optical array
154 probes, such as the 2D-S and HVPS3, use a laser beam between probe arms directed onto
155 an array of photo-diodes to observe cloud particles during flight (Fig. 1). The 2D-S has
156 128 diodes with a 10 μm resolution and the HVPS3 has 128 diodes with a 150 μm
157 resolution. Ice crystals and water droplets passing through the laser beam between the
158 arms block light, causing reduced illumination on the photo-diode array. Images are
159 produced when at least one array element is “shadowed” (*i.e.* reduced in intensity by
160 50%). The sampling frequency of the photo-detector array is adjusted using the measured
161 true air speed to produce correctly scaled cloud particle images. When cloud particle
162 concentrations are high, the 2D-S probe may not have sufficient time to off-load the array

163 buffer, which results in reduced probe activity (Lawson *et al.* 2006b). CAPE2015 has no
164 “dead time” issues as the particle concentration is low enough that the probe’s activity is
165 100% during all flights analyzed.

166 The Nevzorov probe is a hot-wire instrument with sensors to measure cloud liquid
167 and total (liquid + ice) water content (Korolev *et al.* 1998). The total water content sensor
168 uses a conical receiver to collect both liquid water droplets and ice crystals, while the
169 liquid water content sensor uses a round wire to collect droplets but very few ice
170 particles. Both sensors have corresponding reference sensors that are exposed to the
171 airflow but not cloud particles. The additional power required to maintain constant
172 temperature for particle sensors compared to reference sensors is directly related to water
173 mass. Mass measurements and Aircraft true airspeed are used to determine liquid and
174 total water content. Ice water content is not directly measured but calculated by
175 subtracting the liquid water content from the total water content. Nevzorov probe data
176 processing uses multiple linear regressions of the measured static pressure and indicated
177 airspeed to obtain a per-flight calibration, and an automatic baseline correction ensures
178 out-of-cloud water content is zero (Delene *et al.* 2019). The uncertainty of Nevzorov
179 measurements increases with hydrometeor size because large ice crystals may bounce out
180 of the conical receiver, while large water droplets may not evaporate completely before
181 bouncing from the conical receiver or shedding from the round wire.

182 In recent years, efforts have been made to collectively document the uncertainties
183 associated with optical cloud microphysical probes (Baumgardner *et al.* 2017). These
184 uncertainties include the possibility of particles counted in the wrong size channel

185 (Korolev *et al.* 1991; Baumgardner and Korolev 1997), sizing uncertainty for ice particles
186 outside of the focal volume (Connolly *et al.* 2007), approximation of irregular ice
187 particles as spheres (Wu and McFarquhar 2016), and particle coincidence (Cooper 1988;
188 Lance 2012; Johnson *et al.* 2014). These uncertainties are accounted for as much as
189 possible in the data processing and analysis methodology. Additionally, splashing of
190 water droplets and the shattering of ice crystals can cause measurement errors; hence,
191 anti-shattering probe tips and data processing methods have been employed to minimize
192 such issues.

193 **3. Data Processing**

194 The 2D-S and HVPS3 images are processed to obtain particle concentrations using
195 the sample volume (*SV*) given by

$$SV = DOF * w * TAS * t , \quad (2)$$

196 where *DOF* is the depth of field, *w* is the effective width of the photo-diode array, *TAS* is
197 the aircraft's true airspeed measured by a pitot tube, and *t* is elapsed time (McFarquhar *et*
198 *al.* 2017). The depth of field (Fig. 1) is the region along the laser beam where particles
199 are sufficiently within focus to create a clear shadow on a photo-diode (Korolev 2007).
200 *DOF*w* is the sample area, while *TAS*t* provides the third dimension in determining *SV*.
201 The nose gust boom measured TAS and left wing pitot tube (Fig. 2) measured TAS agree
202 within 3% for the CAPE2015 field project.

203 Quality control conducted during the CAPE2015 field project involved instrument
204 maintenance and performance checks. Instrument maintenance included cleaning the
205 outside windows on all optical probes before each flight. Performance checks included
206 reviewing the voltages of the first and last (edge) photo-diodes in the cloud probe arrays

207 and ground testing instruments with spray water to ensure correct performance. To
208 minimize the duration of measurement issues cloud particle data are reviewed during and
209 following each research flight. Cloud particle data are monitored by cabin scientist during
210 flight for instrument malfunctions such as stuck-bits (elements with persistently reduced
211 voltages that continuously indicate shadowing) on the photo-diode arrays. To enable
212 timely post-flight data review, the open source Airborne Data Processing and Analysis
213 (ADPAA) software package (Delene 2011) is used to automatically process and visualize
214 data after each flight.

215 ADPAA assists with post-project quality assurance that is conducted by experienced
216 instrument operators to ensure the data set is satisfactory for the intended scientific
217 analysis. For example, the two-dimensional probe images are reviewed for diode
218 malfunctions, such as stuck-bits, that would be problematic for software processing. Data
219 quality issues are documented in an “edit” file, and the parameter’s value is replaced with
220 the missing value code for the affected time interval. Even with rigorous instrument
221 quality control and assurance, data set problems can still occur. For example, the liquid
222 cloud droplet size spectrum measured by a CDP is inconsistent (*i.e.* a factor of ten low)
223 compared to the 2D-S size spectrum in the overlapping region. Misalignment of the CDP
224 laser discovered after the CAPE2015 project makes the CDP measurements validity
225 questionable; therefore, only the 2D-S and HVPS3 instruments are used to create a
226 combined size spectrum.

227 All CAPE2015 two-dimensional optical array probe data are automatically processed
228 using ADPAA code (Delene *et al.* 2020) that interfaces with the System for Optical Array

229 Probe Data Analysis Version 2 (SODA2) software package (Bansemer 2013). Data
230 processing uses SODA2's fast-circle method for determining particle diameter from two-
231 dimensional probe images. The fast-circle method uses the diameter of the smallest
232 particle-encompassing circle to represent the particle diameter (Wu and McFarquhar
233 2016). A data processing correction for out-of-focus droplets (Korolev 2007) is used
234 during periods when only liquid droplets are sampled. A liquid water droplet acts as a
235 lens, causing light refraction that results in a bright spot (known as a Poisson spot) in the
236 center of the particle shadow. This results in out-of-focus particles having larger
237 shadowed areas. SODA2's water processing corrects for these excessively large particle
238 diameters by comparing the Poisson spot area to the area of the whole particle shadow.
239 This area ratio is used to reduce the droplet diameter to the correct size. Out-of-focus ice
240 crystals also have Poisson spots; however, due to their irregular shape, a similar
241 correction cannot be made and is a potential source of error in this study. Even when
242 using Korolev anti-shatter tips, bursts of particles over a short sampling period are likely
243 shattering artifacts (Field *et al.* 2006); therefore, SODA's shattering artifact rejection
244 methodology is used for all CAPE2015 data processing.

245 SODA2 processing of the CAPE2015 2D-S and HVPS3 images uses the center-of-
246 mass-in method (Heymsfield and Parrish 1978) to obtain particle concentrations. Center-
247 of-mass-in processing calculates concentration using only particles where the estimated
248 center of the particle shadow is between the edge elements of the photo-diode array. An
249 ADPAA script merges 2D-S horizontal arms size channels (5 to 1000 μm) and HVPS3
250 (1000 to 30 000 μm) size channels produced by SODA2 to create a combined particle

251 size distribution (Table 1). The full reconstruction method has also been used to process
252 and analyze CAPE2015 data (Wagner 2020). Full particle reconstruction includes all
253 particles instead of only reconstructing particles where the center of mass is determined
254 to be within the edge of the photo-diode array. An image with only a couple of edge
255 elements shadowed is interpreted as a small particle using the full reconstruction method,
256 while the center-of-mass-in method excludes such particles. While edge element images
257 are not that frequent, a few small particles have a large effect on the 5 to 105 μm diameter
258 size spectrum since the sample volume within this size range is so small. Small particles
259 have a limited depth of field for in-focus particles, which results in the small sample
260 volume. Additionally, determining particle diameter using an image where most of the
261 particle is outside the photo-diode array results in a large uncertainty for irregularly
262 shaped particles since accurate reconstruction is difficult. Furthermore, using full particle
263 reconstruction for CAPE2015 is not necessary since HVPS3 measurements are available
264 to cover the larger particle size range, and the observed cirrus clouds do not contain many
265 particles large enough to be excluded by center-of-mass-in HVPS3 processing. Hence,
266 the center-of-mass-in method is used exclusively for the following analysis.

267 **4. Methodology**

268 Cloud particles are typically much larger than the wavelengths (905 nm and 1550 nm)
269 of the OID, especially particles in cirrus cloud anvils. The ratio of particle diameter to
270 wavelength defines the type of light scattering (geometric, Mie, or Rayleigh) and is
271 known as the size parameter α , which is given by:

$$\alpha = \frac{\pi D}{\lambda}, \quad (3)$$

272 where D is the cloud particle diameter, and λ is the wavelength of incident light (Hulst
273 1981). Light scattering is in the geometric regime when the size parameter is greater than
274 100, in the Mie regime when the size parameter is between 0.1 and 100, and in the
275 Rayleigh regime when the size parameter is less than 0.1 (Bohren and Huffman 1983).
276 Most size channels of the combined cloud probe spectrum are in the geometric scattering
277 regime (Table 1). However, determining backscatter coefficients from particle size
278 distributions using geometric optics methods produces inaccuracies due to a lack of
279 higher-order scattering terms (Zhou and Yang 2015; Yang and Liou 1995). While Mie
280 theory strictly applies to spherical particles, studies have found that uncertainties in using
281 spherical Mie theory code for aspherical scatterers are far less than uncertainties
282 associated with measurements of cloud particle sizes (Cairo *et al.* 2011). Compared to
283 spherical particles, aspherical particles tend to increase side scattering and reduce forward
284 and backward scattering, which can result in an over estimation of backscatter
285 coefficients by a factor of four (Mishchenko *et al.* 1996; Cairo *et al.* 2011). Considering
286 the low backscatter coefficient uncertainty when a sufficient number of terms in the Mie
287 Theory series approximations are used, the entire cloud probe derived size range is
288 processed using Mie theory.

289 Backscatter coefficients depend on particle scattering efficiency at 180° (backscatter
290 efficiency), the number concentration, and the particle size (Bohren and Huffman 1983).
291 The backscatter coefficient equation (Zhang *et al.* 2015) is given by

$$\beta_{ECP} = \sum_{i=1}^{i=\max} Q_i \eta_i \pi r_i^2, \quad (4)$$

292 where β_{ECP} is derived backscatter coefficient using the combined particle size distribution
293 from external cloud probes (ECP), i is particle channel number (see Table 1), n_i is number
294 of particles in channel i , Q_i is scattering efficiency at 180° for channel i , and r_i is particle
295 radius of the channel's midpoint. Backscatter efficiency indicates effectiveness of a
296 particle at scattering in the 180° direction with regard to incident light. Backscatter
297 efficiency is calculated for 100 000 particle diameters spanning 1 μm to 30 mm using the
298 Python based software, MiePlot (Laven 2018). Backscatter efficiency calculations use
299 20°C for the medium temperature, 905 nm for the incident light wavelength, and
300 refractive indices of $1.3263 + 5.6 \times 10^{-7}j$ for water at 20°C (Kedenburg *et al.* 2012) and
301 $1.3031 + 5.6 \times 10^{-7}j$ for ice (Warren and Brandt 2008). The refractive indices depend not
302 only on incident wavelength but also on particle temperature (Wesely 1976). However,
303 sensitivity tests using 0°C and 10°C water refractive indices show a difference of less
304 than 1% for particle diameters up to 105 μm . Correct utilization of MiePlot for
305 determination of water backscatter efficiency has been confirmed by obtaining results
306 comparable to Fig. 61 of Hulst 1981 and Fig. 1 of Lolli *et al.* 2013.

307 Backscatter efficiency is averaged for all particle diameters within each channel
308 (Shishko *et al.* 2020) in the combined particle size spectrum (Fig. 3). Diameters are
309 distributed log-normally between 1 μm and 30 mm, with intervals ranging from 0.0001
310 μm between the smallest diameters to 3 μm between the largest diameters. Averaging
311 over channel intervals smooths out rapid changes in backscatter efficiencies with
312 diameter. As a result, the backscatter efficiencies for water and ice are nearly constant
313 (within approximately 10%) for particle diameters up to 105 μm (the upper limit of size

314 bin 10 in Table 1). Above 105 μm , water has a backscatter efficiency that increases, while
 315 ice has a backscatter efficiency that decreases. There is a backscatter efficiency dip
 316 around 10 000 μm diameter, which is likely due to destructive interference of surface
 317 waves. Backscatter can be conceptualized as a light wave scattering back to the source by
 318 exiting at a 180° angle after traveling around the droplet's surface, sometimes traversing
 319 around many times. The existence of surface waves in droplets has been directly
 320 observed (Fahlen and Bryant 1966) and is responsible for the well-known "glory
 321 phenomenon" (Gillis *et al.* 1998) that is produced by strong light backscattering. Surface
 322 waves traveling around the droplet a variable number of times can destructively interfere
 323 resulting in rapid backscatter efficiency changes as seen in Fig. 3 (Hovenac and Lock
 324 1992). While interesting, the backscatter efficiency dip around 10 000 μm diameter is
 325 irrelevant for this study since observed water droplets are much smaller. For more
 326 information about the effects of surface waves on light scattering, see Chýlek *et al.* 1980.

327 Uncertainty in the backscatter coefficient ($\delta\beta_{ECP}$) is derived using a weighted error
 328 propagation in quadrature method (Berendsen 2011):

$$\delta\beta_{ECP} = \sum_{i=1}^{i=ma x} \sqrt{(Q_i \pi r_i^2 \delta\eta_i)^2 + (2\eta_i Q_i \pi r_i \delta r_i)^2}, \quad (5)$$

329 where $\delta\eta_i$ is concentration uncertainty for channel i and δr_i is particle radius uncertainty
 330 for channel i . Poisson statistics determine absolute uncertainty in concentration:

$$\delta\eta_i = \eta_i * \max_{i=1}^{i=ma x} \left(\frac{1}{\sqrt{N_i}} \right), \quad (6)$$

331 where N_i is counted particle number per channel (Horvath *et al.* 1990). Another example
 332 of applying Poisson statistics to cloud probe analysis can be found in Baumgardner *et al.*

333 2014. One half the channel width is used as the particle radius uncertainty, which is a
334 lower bound on the uncertainty. Additional factors could result in a larger uncertainty. For
335 example, particles outside the depth of field appear too large and hence not within the
336 correct size channel (O’Shea *et al.* 2019).

337 The 1Hz OID backscatter coefficient uncertainty ($\delta\beta_{OID}$) is the standard deviation of
338 the 5 Hz OID data. The standard deviation includes some natural variability, as the
339 aircraft traverses different cloud conditions, in addition to random uncertainty; hence, the
340 uncertainty is an upper bound. OID and ECP agreement is considered to occur when the
341 measurement difference is less than three standard deviations (Berendsen 2011), which is
342 calculated using:

$$\sigma_3 = 3\sqrt{(\delta\beta_{OID})^2 + (\delta\beta_{ECP})^2}, \quad (7)$$

343 Thus, a time series plot of the OID and ECP backscatter coefficient difference is useful to
344 determine periods of measurement agreement and disagreement. Neither (5) nor (7)
345 include any systematic errors (*e.g.* uncertainty in scattering efficiency).

346 **5. Results**

347 OID backscatter coefficients are compared to 1 Hz backscatter coefficients derived
348 from the external cloud probes. Case study analysis and discussion is done on four, 60 s,
349 CAPE2015 flight segments before examining the larger CAPE2015 data set. The cases
350 (Table 2) are at four different temperatures (+7°C, +4°C, -33°C and -46°C), which
351 provide two warm cloud cases and two cold cloud cases at constant flight heading and
352 altitude (Fig. 4). The warm cases (Fig. 4A and 4B) are at approximately 3 km altitude
353 over the ocean, just off the east coast of Florida. The warm cloud cases have small liquid

354 droplets that are not observable on radar (Table 2). The +7°C case occurred early in the
355 flight while waiting for air traffic control climb permission. Similarly, the +4°C case also
356 occurred before ascending to sample cirrus clouds. As expected for these warm
357 temperatures, the 2D-S images (Fig. 4A and 4B) show small spherical droplets. Many
358 droplets are out-of-focus, which requires special data processing to size correctly. The
359 cold cases (Fig. 4C and 4D) occurred above 9 km in cirrus cloud anvils. Melbourne radar
360 observations has cloud bases at 1000 m MSL (Table 2) for both cold cloud cases, which
361 indicates sampling is above the stratus rain region, instead of the cirrus anvil outflow
362 region of the storm. Cloud tops are located at 11 000 m MSL for the -33°C case, and 15
363 000 m MSL for the -46°C case. The 2D-S images show mostly irregularly shaped
364 particles indicative of ice crystals. The -33°C case has some small particles appearing
365 round, which could indicate liquid water in the cloud. Many crystals are out-of-focus;
366 however, special data processing software does not exist to correct the crystal size.

367 Cloud probe images (2D-S and HVPS3) are processed and combined to create a 1 Hz
368 particle size spectrum. The particle size spectrum is used to derive backscatter
369 coefficients (4) and uncertainty (5). The absolute uncertainty is greatest for the +7°C case
370 (Fig. 5A) because the backscatter coefficient magnitude is ten times the +4°C case and
371 one hundred times the cold cases. Fig. 6A shows that OID and ECP backscatter
372 coefficients are in agreement (within three standard deviations) at all times for the +7°C
373 case. The greatest difference occurs at 69 520 seconds from midnight (sfm), where the
374 ECP backscatter coefficient is twice the OID's. Overall, the +7°C case ECP backscatter
375 coefficient is typically higher than the OID. The +7°C water cloud contains high

376 concentrations of small droplets (*i.e.* 20 μm mean diameter), with the majority of the
377 calculated backscatter due to droplets less than 30 μm (Fig. 7).

378 Figure 5B shows that the +4°C case has ECP backscatter coefficients that vary with
379 the OID backscatter coefficient; however, the ECP backscatter coefficient is consistently
380 lower. The OID and ECP backscatter coefficients agree within uncertainties (Fig. 6B)
381 throughout most of the period; however, the OID backscatter coefficients are
382 approximately twice the ECP backscatter coefficients at 57 864 sfm and 57 878 sfm. The
383 difference changes little because the particle concentration (Fig. 7A) and mean diameter
384 (Fig. 7B) are approximately constant. Compared to the +7°C case, the concentration is an
385 order of magnitude less, and the mean diameter is greater, being approximately 50 μm
386 instead of 10 μm . Many of the observed drops are from 30 μm to 70 μm , with the particle
387 size distribution peaking at approximately 50 μm . Particles from 100 to 300 μm diameter
388 are one hundred times more plentiful than in the +7°C case.

389 For the -33°C case (Fig. 5C and Fig. 6C), the OID and ECP backscatter coefficients
390 are in agreement for the first 20 s. Similarly to the +4°C case, the OID backscatter
391 coefficient is consistently higher than that ECP backscatter coefficient. However, around
392 71 735 sfm there is a sudden change in backscatter coefficient agreement that
393 corresponds to an increase in mean particle size and concentration. Figure 7A shows
394 particle concentration increasing from approximately 0.02 cm^{-3} to 0.2 cm^{-3} , and Fig. 7B
395 shows the mean particle diameter increasing from 300 μm to slightly over 1000 μm
396 around the 71 735 sfm change. For the last 30 s, the OID backscatter coefficient is
397 approximately twice the ECP backscatter coefficient, with disagreement exceeding three

398 standard deviations. The particle size spectrum (Fig. 7C) and backscatter coefficient (Fig.
399 7D) are much broader and flatter than in the warm cloud cases. Figure 7D indicates the
400 majority of the backscatter coefficient is due to particles from 200 to 3000 μm in
401 diameter.

402 The -46°C case (Fig. 5D) has the smallest differences between the backscatter
403 coefficients. For the first 40 s, the ECP derived backscatter coefficient is nearly equal to,
404 but consistently less than, that of the OID; however, both measurements exhibit the same
405 temporal trends. For the last half of the period, the backscatter coefficients are shown by
406 Fig. 6D to always be in agreement. As Fig. 7B shows, the mean particle diameter is
407 constant at approximately 500 μm , with a decrease at the end of the period. Both the -
408 46°C case and -33°C case show 2D-S images with large, irregularly shaped particles (Fig.
409 4D and 4C, respectively). The -46°C case has small particles that are irregular in shape,
410 while the -33°C case contains small particles that appear round.

411 There is a strong correlation (R^2 of 0.90) between β_{ECP} versus β_{OID} with the linear fit
412 line being slightly greater than one-to-one (Fig. 8.) Figure 9 shows the total water content
413 (TWC) versus backscatter coefficient has a power-law relationship. The Backscatter-
414 TWC relationship indicates the OID instrument is sensitive to TWC over a wide range of
415 cloud conditions, including in clouds with particle concentrations as low as 0.02 g m^{-3} .
416 Additionally, the OID is sensitive to small values of TWC (plot insert in Fig. 9) in thin ice
417 clouds, which is an important characteristic for deployment on high flying aircraft. The
418 OID has less scatter than the ECP for the Backscatter-TWC plots, likely due to the larger
419 sample volume of the OID. Figure 10 includes all data greater than 0°C and less than -

420 20°C for the complete case study flights. Data between 0°C and 20°C are omitted to
421 exclude strongly mixed-phase cloud conditions. Figure 10 shows much more scatter
422 between the ECP and OID backscatter coefficients than Fig. 8. Unlike Fig. 8, the trend of
423 Fig. 10 indicates the ECP produces higher values than the OID as backscatter coefficients
424 increase. Similarly, Fig. 10 shows more scatter between the OID backscatter coefficient
425 and the Nevzorov probe TWC than seen in Fig. 9 (R^2 of 0.74).

426 **6. Discussion**

427 The +7°C case has the largest backscatter coefficient and the only case where ECP
428 derived backscatter coefficient is larger than the OID measurement. This is due to high
429 droplet concentrations saturating the OID above its detection limit of $22 \text{ km}^{-1} \text{ sr}^{-1}$. The
430 OID's limited dynamic range in a dense cloud of small water droplets is not a serious
431 liability since sensing ice particle concentration is the main measurement objective and
432 warm water clouds do not produce ice particle icing. Environments containing severe
433 liquid water icing conditions would be flagged without having to exceed measurements
434 of $22 \text{ km}^{-1} \text{ sr}^{-1}$. Note that the cumulus cloud sampled in the +7°C case has a large water
435 content (Table 2), and the backscatter coefficients to water content comparisons indicates
436 the OID is able to measure over 1.0 g m^{-3} before saturation (Fig. 9).

437 Excluding the +7°C case, ECP backscatter coefficients are consistently lower than
438 those measured by the OID (Fig. 5B, 5C, and 5D). The consistent difference between the
439 OID and ECP suggests a possible systematic error. Two-dimensional cloud imaging
440 probes (Fig. 1) have several factors that can bias sizing and counting of particles. For
441 example, particle diameters less than $100 \mu\text{m}$ are difficult for the 2D-S to measure due to

442 the small depth of field, which could result in lower backscatter coefficients than those
443 measured by the OID. However, the 2D-S liquid water content (LWC) is larger than the
444 Nevzorov probe measurements for the CAPE2015 field project. It seems the Nevzorov
445 LWC is low, which may result from an inability to fully capture and/or evaporate the
446 largest water droplets. The OID measurements may have a bias despite no indication of
447 malfunctions. Another possibility is the OID receiving backscatter from particles too
448 small to be measured by the two-dimensional cloud imaging probes; however, Fig. 7D
449 indicates low backscatter coefficient contribution from the smallest sized channels..
450 Additional measurements with carefully calibrated instruments are necessary to resolve
451 the discrepancy between the OID and ECP for liquid water droplets; however, the OID
452 and ECP measurements do agree within the calculated uncertainties most of the time for
453 liquid clouds (Fig. 6).

454 There are other possible errors which affect both liquid water and ice water
455 measurements. A bias in concentration could be due to an error in air speed used for
456 determining the sampling volume (2). However, the aircraft's air speed error is estimated
457 to be between 1% and 3% based on measurement comparisons, which is too small to
458 account for the bias. Another error source may be coupling probes to the ambient
459 environment. Air flow around instrument pylons can be affected even when probes are
460 placed well in front of the wing's leading edge (Baumgardner 1984). Pressure changes
461 and streamlines alter particle flow around both wings and instruments, with small
462 particles being most heavily affected (Spanu *et al.* 2020). This phenomenon results in
463 lower measured concentrations of small particles. Another possible concentration bias is

464 in processing asynchronous 2D probe images to calculate the sample area. Errors in
465 determining sample area are size dependent and larger for small particles (Korolev *et al.*
466 2013b); therefore, such errors are more important for the +7°C and +4°C cases.

467 A sample area error affects particle concentration, which has the larger uncertainty
468 contribution. The +4°C case (Fig. 9) has an average contribution to uncertainty (6) of
469 $0.36 \text{ km}^{-1} \text{ sr}^{-1}$ from particle concentration, while only $0.04 \text{ km}^{-1} \text{ sr}^{-1}$ from particle size.
470 Similarly, the -46°C case (Fig. 5D) has uncertainty of $0.40 \text{ km}^{-1} \text{ sr}^{-1}$ from concentration
471 and only $0.05 \text{ km}^{-1} \text{ sr}^{-1}$ from particle size. Hence, the primary contributor to total
472 uncertainty is fluctuation in concentration. Concentration uncertainty can be reduced by
473 averaging over longer time periods; however, systematic differences between the OID
474 and ECP would not be reduced.

475 Bias in calculated sample volume cannot explain the change in agreement between
476 OID and ECP backscatter coefficients that occurred between 71 730 sfm and 71 740 sfm
477 for the -33°C case (Fig. 4C, 5C, and 6C). Onset of the discrepancy could be due to a
478 change in the particle size spectrum (Fig. 11). Manually reviewing 2D-S and HVPS3
479 images indicates an increased number of larger particles between the first and last 20 s of
480 the -33°C case. This change in particle size distribution is believable since there is a
481 smooth decrease in concentration with increasing size. Furthermore, the 2D-S/HVPS3
482 particle size distribution is similar to the Two Dimensional Cloud (2D-C) probe (Fig. 2)
483 distribution (Fig. 11), and performance checks conducted by the manufacturers after
484 CAPE2015 found no measurement issues. Additionally, there is no reason not to believe

485 the OID measurements as a manufacturer's review indicated no measurement issues.
486 Therefore, both the OID and ECP measurements seem to be valid for the -33°C case.

487 A notable difference between the -33°C and -46°C cases is LWC measured by the
488 Nevzorov probe (Fig. 12). The Nevzorov probe measurement for the -46°C case has near
489 zero LWC, as expected for a temperature below homogeneous freezing. However, the
490 Nevzorov probe measurement indicates a mixed phase cloud for the -33°C case. While
491 there is LWC data shown for the entire -33°C case, LWC increases from an average of
492 0.022 g m^{-3} to 0.027 g m^{-3} (~30% of the TWC) just after disagreement between
493 backscatter coefficients begins. It should be noted that while the Nevzorov probe has a
494 collection efficiency of nearly 1 for droplets with a diameter less than $100 \mu\text{m}$ (Korolev
495 *et al.* 1998), collection efficiency is approximately 0.5 for clouds with a mean particle
496 volume diameter of $150 - 200 \mu\text{m}$ (Biter *et. al* 1987). During the disagreement period,
497 there are significantly more particles with diameters from 150 to $200 \mu\text{m}$ (Fig. 11), which
498 would require a greater, and not readily available, correction to Nevzorov probe LWC
499 measurements.

500 Even at temperatures as low as -33°C, supercooled liquid water droplets can still exist
501 (Rosenfeld and Woodley 2000). Supercooled liquid water droplets have even been
502 observed by the same OID at temperatures as low as -30°C in Anderson and Ray 2019.
503 Similarly to Anderson and Ray 2019, such supercooled liquid water droplets are evident,
504 but not proven, by the round particles seen in 2D-S images taken at the LWC
505 measurement peak (Fig. 4C). Additionally, the Rosemount Icing Detector (Fig. 2) rod
506 frequency (not shown) indicates the presence of LWC. We speculate that the presence of

507 supercooled liquid water droplets in the -33°C case results in larger OID backscatter
508 coefficients due to higher (see Q Ratios in Table 1) water backscatter efficiency (Fig. 3).
509 Using liquid water scattering efficiencies to calculate ECP backscatter coefficients for
510 particles less than 500 μm results in ECP/OID agreement for the -33°C case. Accounting
511 for mixed phase conditions in ECP backscatter coefficients would require a methodology
512 able to simultaneously utilize a particle size spectrum for both liquid water and ice, which
513 is beyond the scope of this study.

514 **7. Conclusions**

515 A backscatter coefficient comparison is conducted for both warm and cold clouds of
516 an *in-situ* lidar (OID) and estimates from externally mounted cloud particle probes
517 (ECP). ECP derived backscatter coefficients are consistently lower than OID
518 measurements for the +4°C, -33°C, and -46°C cases, suggesting a systematic bias in
519 either or both data sets. However, the ECP derived backscatter coefficient is higher than
520 OID measurement for the +7°C case due to OID saturation. ECP backscatter coefficients
521 are less than three standard deviations from OID measurements, indicating agreement for
522 the +7°C case and most of the +4°C and -46°C cases. The -33°C case has disagreement
523 for 35 s out of 60 s, which is likely due to using ice scattering efficiencies for all particles
524 when small particles are liquid. All case comparisons show qualitatively that backscatter
525 coefficients are a suitable proxy for liquid and ice water contents as low as 0.02 g m⁻³. A
526 comparison between OID and ECP backscatter coefficients to Nevzorov probe total water
527 content for all times during four CAPE2015 flights (Fig. 10) has a correlation above 0.7.
528 Considering the measurement uncertainties, the case study analysis, and overall flight

529 comparison, the OID is a useful tool in detecting dangerous ice particle icing conditions,
530 even at low concentrations.

531 The CAPE2015 field project analysis could be expanded to include additional field
532 projects. Additionally, future work could include both the 905 nm and 1550 nm OID
533 wavelengths. Using both wavelengths would allow two parameters of cloud particle size
534 distributions to be determined, helping to obtain a total water content. Additionally, OID
535 polarization measurements could distinguish the liquid/ice fraction of clouds (Yang *et al.*
536 2003). New instrumentation, such as the Particle Habit Imaging and Polar Scattering
537 (PHIPS) probe (Schön *et al.* 2011) deployed during the CapeEx19 Florida field project,
538 would be very useful in determining the fraction of liquid water in mixed phase clouds.
539 Quantifying the liquid water fraction of mixed phase clouds would allow for creation of
540 both liquid and ice 1 Hz particle size distributions, so liquid and ice scattering efficiencies
541 could simultaneously be used to obtain the backscattering coefficient. PHIPS data would
542 also aid in the identification of ice particle habits. Knowing the ice particle habits would
543 allow for more accurate scattering calculations to be utilized (Yang *et al.* 2005).

544 **8. Data and Software Availability**

545 The paper's data set is freely accessible online through the Chester Fritz Library's
546 data collection (Wagner and Delene 2020a). Archived data consists of 1 Hz data from
547 four Florida flights in 2015. Data set measurements include the Two-Dimensional Stereo
548 probe (2D-S), High-Volume Precipitation Spectrometer Version Three (HVPS3) probe
549 and Nevzorov probe. 2D-S and HVPS3 spectrum are combined to create a single particle
550 size distribution spanning both probe size ranges. Backscatter coefficients are computed

551 from this composite size spectrum. Atmospheric variables such as pressure, temperature,
552 dew point, and wind velocity are also included in the data archive.

553 ADPAA software used to process the raw data is freely available from a software
554 repository (Delene *et al.* 2020). Also, specialized software used in the paper’s analysis is
555 available in a publicly accessible repository (Wagner and Delene 2020b). Software
556 processing configuration details are documented in a work-flow script entitled
557 “oid_analysis_workflow” (Wagner 2020). The work-flow script contains execution calls
558 to ADPAA modules used to process and analyze the paper’s data set. Whereas ADPAA
559 processes data from many field projects, the work-flow script applies only to this paper’s
560 analysis. The MiePlot software package (Laven 2018) used to calculate backscatter
561 efficiencies is readily available online.

562 **Acknowledgments**

563 First author, Shawn Wagner, conducted data analysis and lead manuscript writing. Co-
564 author David Delene developed the project’s design and scope. David Delene headed
565 external cloud probe analysis. Both authors reviewed and edited the manuscript. Opinions
566 expressed in this paper are those of the authors and do not reflect opinions of others who
567 aided in this research.

568 We are grateful to the National Center for Atmospheric Research (NCAR), and the
569 lead developer Aaron Bansemer, for making available the SODA software used in this
570 research. Thank you to NASA for use of 2D-S, HVPS3, and Nevzorov probe instruments
571 during the CAPE2015 field project. Kaare Anderson provided processed OID data for
572 CAPE2015. The CAPE2015 aircraft flight crew members included flight engineers Jamie

573 Ekness (Graduate Student), Krysztof Markowicz (Graduate Student) and Nicholas Gapp
574 (Undergraduate Student), flight scientist David Delene, and research pilots Wayne
575 Schindler and Jonathan Sepulveda. Thanks to Andrew Detwiler for providing comments
576 on draft versions of the paper. CAPE2015 was sponsored by the Naval Surface Warfare
577 Center, Dahlgren Division, grant (UND0020625, UND0020633, UND0020634). Funding
578 to conduct data analysis was provided by the North Dakota Department of Commerce
579 (UND0021191).

580 **References**

- 581 Airworthiness Directives, 2013: The Boeing Company Airplanes. *Federal Register*.
- 582 <https://www.federalregister.gov/documents/2013/11/27/2013-28638/airworthiness->
- 583 directives-the-boeing-company-airplanes (Accessed January 21, 2020).
- 584 Anderson, K. J., and M. D. Ray, 2019: *SLD and Ice Crystal Discrimination with the*
- 585 *Optical Ice Detector*. SAE International.
- 586 Bansemer, Aaron, 2013: Software for OAP Data Analysis Version 2. *Github*,
- 587 <https://github.com/abansemer/soda2>.
- 588 Baumgardner, D., 1984. The effects of air-flow distortion on aircraft measurement: A
- 589 workshop summary. *Bulletin Of The American Meteorological Society*, **65**, 1212-
- 590 1213.
- 591 —, and A. Korolev, 1997: Airspeed Corrections for Optical Array Probe Sample
- 592 Volumes. *J. Atmos. Oceanic Technol.*, **14**, 1224–1229, <https://doi.org/10.1175/1520->
- 593 [0426\(1997\)014<1224:ACFOAP>2.0.CO;2](https://doi.org/10.1175/1520-0426(1997)014<1224:ACFOAP>2.0.CO;2).
- 594 —, and Coauthors, 2017: Cloud Ice Properties: In Situ Measurement Challenges.
- 595 *Meteorological Monographs*, **58**, 9.1-9.23,
- 596 <https://doi.org/10.1175/AMSMONOGRAPHS-D-16-0011.1>.
- 597 —, R. Newton, M. Krämer, J. Meyer, A. Beyer, M. Wendisch, and P. Vochezer, 2014:
- 598 The Cloud Particle Spectrometer with Polarization Detection (CPSPD): A next
- 599 generation open-path cloud probe for distinguishing liquid cloud droplets from ice
- 600 crystals. *Atmospheric Research*, **142**, 2–14,
- 601 <https://doi.org/10.1016/j.atmosres.2013.12.010>.

602 Berendsen, H. J. C., 2011: A Student's Guide to Data and Error Analysis. *Cambridge*
603 *Core*, <https://doi.org/10.1017/CBO9780511921247>.

604 Beswick, K., D. Baumgardner, M. Gallagher, A. Volz-Thomas, P. Nedelec, K.-Y. Wang,
605 and S. Lance, 2014: The backscatter cloud probe; a compact low-profile autonomous
606 optical spectrometer. *Atmospheric Measurement Techniques*, **7**, 1443–1457,
607 <https://doi.org/10.5194/amt-7-1443-2014>.

608 ———, and Coauthors, 2015: Properties of Small Cirrus Ice Crystals from Commercial
609 Aircraft Measurements and Implications for Flight Operations. *Tellus B: Chemical*
610 *and Physical Meteorology*, **67**, 27876, <https://doi.org/10.3402/tellusb.v67.27876>.

611 Biter, C. J., J. E. Dye, D. Huffman, and W. D. King, 1987: The Drop-Size Response of
612 the CSIRO Liquid Water Probe. *J. Atmos. Oceanic Technol.*, **4**, 359–367,
613 [https://doi.org/10.1175/1520-0426\(1987\)004<0359:TDSROT>2.0.CO;2](https://doi.org/10.1175/1520-0426(1987)004<0359:TDSROT>2.0.CO;2).

614 Bohren, C. F., and D. R. Huffman, 1983: *Absorption and scattering of light by small*
615 *particles*. Wiley, xiv+530 pp.

616 Bravin, M., J. W. Strapp, and J. Mason, 2015: *An Investigation into Location and*
617 *Convective Lifecycle Trends in an Ice Crystal Icing Engine Event Database*. SAE
618 International.

619 Cairo, F., G. D. Donfrancesco, M. Snels, F. Fierli, M. Viterbini, S. Borrmann, and W.
620 Frey, 2011: A comparison of light backscattering and particle size distribution
621 measurements in tropical cirrus clouds. *Atmospheric Measurement Techniques*, **4**,
622 557–570, <https://doi.org/10.5194/amt-4-557-2011>.

623 Chýlek, P., J. T. Kiehl, M. K. W. Ko, and A. Ashkin, 1980: Surface Waves in Light
624 Scattering by Spherical and Non-Spherical Particles. *Light Scattering by Irregularly*
625 *Shaped Particles*, D.W. Schuerman, Ed., Springer US, 153–164.

626 Connolly, P. J., M. J. Flynn, Z. Ulanowski, T. W. Choularton, M. W. Gallagher, and K. N.
627 Bower, 2007: Calibration of the Cloud Particle Imager Probes Using Calibration
628 Beads and Ice Crystal Analogs: The Depth of Field. *J. Atmos. Oceanic Technol.*, **24**,
629 1860–1879, <https://doi.org/10.1175/JTECH2096.1>.

630 Cooper, W. A., 1988: Effects of Coincidence on Measurements with a Forward Scattering
631 Spectrometer Probe. *J. Atmos. Oceanic Technol.*, **5**, 823–832,
632 [https://doi.org/10.1175/1520-0426\(1988\)005<0823:EOCOMW>2.0.CO;2](https://doi.org/10.1175/1520-0426(1988)005<0823:EOCOMW>2.0.CO;2).

633 Delene, D. J., 2011: Airborne data processing and analysis software package. *Earth Sci*
634 *Inform*, **4**, 29–44, <https://doi.org/10.1007/s12145-010-0061-4>.

635 ———, 2016: Suitability of North Dakota for Conducting Effective Hygroscopic Seeding.
636 *JournalWeaMod*, **48**, 43–67.

637 ———, K. Hibert, M. Poellot, and N. Brackin, 2019: The North Dakota Citation Research
638 Aircraft Measurement Platform. *2019 SAE International Conference on Icing of*
639 *Aircraft, Engines, and Structures*.

640 ———, A. Skow, J. O'Brien, N. Gapp, S. Wagner, K. Hibert, K. Sand, and G. Sova, 30
641 March 2020, Airborne Data Processing and Analysis Software Package (Version
642 3981), Zenodo, doi:10.5281/zenodo.3733448.

643 Fahlen, T. S., and H. C. Bryant, 1966: Direct Observation of Surface Waves on Water
644 Droplets*. *J. Opt. Soc. Am., JOSA*, **56**, 1635–1636,
645 <https://doi.org/10.1364/JOSA.56.001635>.

646 Field, P. R., A. J. Heymsfield, and A. Bansemer, 2006: Shattering and Particle Interarrival
647 Times Measured by Optical Array Probes in Ice Clouds. *J. Atmos. Oceanic Technol.*,
648 **23**, 1357–1371, <https://doi.org/10.1175/JTECH1922.1>.

649 Frey, W., and Coauthors, 2011: In situ measurements of tropical cloud properties in the
650 West African Monsoon: upper tropospheric ice clouds, Mesoscale Convective
651 System outflow, and subvisual cirrus. *Atmospheric Chemistry and Physics*, **11**, 5569–
652 5590, <https://doi.org/10.5194/acp-11-5569-2011>.

653 Gayet, J. F., and Coauthors, 2012: On the observation of unusual high concentration of
654 small chain-like aggregate ice crystals and large ice water contents near the top of a
655 deep convective cloud during the CIRCLE-2 experiment. *Atmospheric Chemistry
656 and Physics*, **12**, 727–744, <https://doi.org/10.5194/acp-12-727-2012>.

657 Gillis, P., C. Deleuze, V. P. Henri, and J. M. Lesceux, 1998: Backscattering of light from a
658 water droplet: The glory effect. *American Journal of Physics*, **50**, 416,
659 <https://doi.org/10.1119/1.12828>.

660 Haggerty, J., and Coauthors, 2018: Detecting Clouds Associated with Jet Engine Ice
661 Crystal Icing. *Bull. Amer. Meteor. Soc.*, **100**, 31–40, [https://doi.org/10.1175/BAMS-](https://doi.org/10.1175/BAMS-D-17-0252.1)
662 [D-17-0252.1](https://doi.org/10.1175/BAMS-D-17-0252.1).

663 Halama, G., M. Ray, K. Anderson, M. Nesnidal, and R. Ide, 2010: Optical Ice Detection:
664 Test Results from the NASA Glenn Icing Research Tunnel. *AIAA Atmospheric and*
665 *Space Environments Conference*, American Institute of Aeronautics and Astronautics.

666 Heymsfield, A. J., 1986: Ice Particle Evolution in the Anvil of a Severe Thunderstorm
667 during CCOPE. *J. Atmos. Sci.*, **43**, 2463–2478, [https://doi.org/10.1175/1520-](https://doi.org/10.1175/1520-0469(1986)043<2463:IPEITA>2.0.CO;2)
668 [0469\(1986\)043<2463:IPEITA>2.0.CO;2](https://doi.org/10.1175/1520-0469(1986)043<2463:IPEITA>2.0.CO;2).

669 —, and L. M. Miloshevich, 1993: Homogeneous Ice Nucleation and Supercooled
670 Liquid Water in Orographic Wave Clouds. *J. Atmos. Sci.*, **50**, 2335–2353,
671 [https://doi.org/10.1175/1520-0469\(1993\)050<2335:HINASL>2.0.CO;2](https://doi.org/10.1175/1520-0469(1993)050<2335:HINASL>2.0.CO;2).

672 —, and J. L. Parrish, 1978: A Computational Technique for Increasing the Effective
673 Sampling Volume of the PMS Two-Dimensional Particle Size Spectrometer. *J. Appl.*
674 *Meteor.*, **17**, 1566–1572, [https://doi.org/10.1175/1520-](https://doi.org/10.1175/1520-0450(1978)017<1566:ACTFIT>2.0.CO;2)
675 [0450\(1978\)017<1566:ACTFIT>2.0.CO;2](https://doi.org/10.1175/1520-0450(1978)017<1566:ACTFIT>2.0.CO;2).

676 —, and Coauthors, 2017: Cirrus Clouds. *Meteor. Monogr.*, **58**, 2.1-2.26,
677 <https://doi.org/10.1175/AMSMONOGRAPHS-D-16-0010.1>.

678 Horvath, H., R. L. Gunter, and S. W. Wilkison, 1990: Determination of the Coarse Mode
679 of the Atmospheric Aerosol Using Data from a Forward-Scattering Spectrometer
680 Probe. *Aerosol Science and Technology*, **12**, 964–980,
681 <https://doi.org/10.1080/02786829008959407>.

682 Hovenac, E. A., and J. A. Lock, 1992: Assessing the contributions of surface waves and
683 complex rays to far-field Mie scattering by use of the Debye series. *J. Opt. Soc. Am.*
684 *A, JOSAA*, **9**, 781–795, <https://doi.org/10.1364/JOSAA.9.000781>.

685 Hulst, H. C. van de, 1981: *Light Scattering by Small Particles*. Corrected Edition edition.
686 Dover Publications, 496 pp.

687 Jensen, M. P., and Coauthors, 2015: The Midlatitude Continental Convective Clouds
688 Experiment (MC3E). *Bull. Amer. Meteor. Soc.*, **97**, 1667–1686,
689 <https://doi.org/10.1175/BAMS-D-14-00228.1>.

690 Johnson, A., S. Lasher-Trapp, A. Bansemer, Z. Ulanowski, and A. J. Heymsfield, 2014:
691 Difficulties in Early Ice Detection with the Small Ice Detector-2 HIAPER (SID-2H)
692 in Maritime Cumuli. *J. Atmos. Oceanic Technol.*, **31**, 1263–1275,
693 <https://doi.org/10.1175/JTECH-D-13-00079.1>.

694 Kedenburg, S., M. Vieweg, T. Gissibl, and H. Giessen, 2012: Linear refractive index and
695 absorption measurements of nonlinear optical liquids in the visible and near-infrared
696 spectral region. *Opt. Mater. Express, OME*, **2**, 1588–1611,
697 <https://doi.org/10.1364/OME.2.001588>.

698 Korolev, A., 2007: Reconstruction of the Sizes of Spherical Particles from Their Shadow
699 Images. Part I: Theoretical Considerations. *J. Atmos. Oceanic Technol.*, **24**, 376–389,
700 <https://doi.org/10.1175/JTECH1980.1>.

701 ———, E. F. Emery, J. W. Strapp, S. G. Cober, and G. A. Isaac, 2013b: Quantification of
702 the Effects of Shattering on Airborne Ice Particle Measurements. *J. Atmos. Oceanic
703 Technol.*, **30**, 2527–2553, <https://doi.org/10.1175/JTECH-D-13-00115.1>.

704 ———, and G. A. Isaac, 2005: Shattering during Sampling by OAPs and HVPS. Part I:
705 Snow Particles. *J. Atmos. Oceanic Technol.*, **22**, 528–542,
706 <https://doi.org/10.1175/JTECH1720.1>.

707 ———, S. V. Kuznetsov, Y. E. Makarov, and V. S. Novikov, 1991: Evaluation of
708 Measurements of Particle Size and Sample Area from Optical Array Probes. *J.*
709 *Atmos. Oceanic Technol.*, **8**, 514–522, [https://doi.org/10.1175/1520-](https://doi.org/10.1175/1520-0426(1991)008<0514:EOMOPS>2.0.CO;2)
710 [0426\(1991\)008<0514:EOMOPS>2.0.CO;2](https://doi.org/10.1175/1520-0426(1991)008<0514:EOMOPS>2.0.CO;2).

711 ———, J. W. Strapp, G. A. Isaac, and E. Emery, 2013a: Improved Airborne Hot-Wire
712 Measurements of Ice Water Content in Clouds. *J. Atmos. Oceanic Technol.*, **30**,
713 2121–2131, <https://doi.org/10.1175/JTECH-D-13-00007.1>.

714 ———, ———, ———, and A. N. Nevzorov, 1998: The Nevzorov Airborne Hot-Wire LWC–
715 TWC Probe: Principle of Operation and Performance Characteristics. *J. Atmos.*
716 *Oceanic Technol.*, **15**, 1495–1510, [https://doi.org/10.1175/1520-](https://doi.org/10.1175/1520-0426(1998)015<1495:TNAHWL>2.0.CO;2)
717 [0426\(1998\)015<1495:TNAHWL>2.0.CO;2](https://doi.org/10.1175/1520-0426(1998)015<1495:TNAHWL>2.0.CO;2).

718 Krämer, M., and Coauthors, 2009: Ice supersaturations and cirrus cloud crystal numbers.
719 *Atmospheric Chemistry and Physics*, **9**, 3505–3522, [https://doi.org/10.5194/acp-9-](https://doi.org/10.5194/acp-9-3505-2009)
720 [3505-2009](https://doi.org/10.5194/acp-9-3505-2009).

721 Kumjian, M. R., S. Mishra, S. E. Giangrande, T. Toto, A. V. Ryzhkov, and A. Bansemer,
722 2016: Polarimetric radar and aircraft observations of saggy bright bands during
723 MC3E. *Journal of Geophysical Research: Atmospheres*, **121**, 3584–3607,
724 <https://doi.org/10.1002/2015JD024446>.

725 Lance, S., 2012: Coincidence Errors in a Cloud Droplet Probe (CDP) and a Cloud and
726 Aerosol Spectrometer (CAS), and the Improved Performance of a Modified CDP. *J.*
727 *Atmos. Oceanic Technol.*, **29**, 1532–1541, [https://doi.org/10.1175/JTECH-D-11-](https://doi.org/10.1175/JTECH-D-11-00208.1)
728 [00208.1](https://doi.org/10.1175/JTECH-D-11-00208.1).

729 Laven, P., 2018: MiePlot. <http://www.philiplaven.com/mieplot.htm> (Accessed January
730 20, 2020).

731 Lawson, R. P., L. J. Angus, and A. J. Heymsfield, 1998: Cloud Particle Measurements in
732 Thunderstorm Anvils and Possible Weather Threat to Aviation. *Journal of Aircraft*,
733 <https://doi.org/10.2514/2.2268>.

734 ———, B. Baker, B. Pilson, and Q. Mo, 2006a: In Situ Observations of the Microphysical
735 Properties of Wave, Cirrus, and Anvil Clouds. Part II: Cirrus Clouds. *J. Atmos. Sci.*,
736 **63**, 3186–3203, <https://doi.org/10.1175/JAS3803.1>.

737 ———, D. O’Connor, P. Zmarzly, K. Weaver, B. Baker, Q. Mo, and H. Jonsson, 2006b: The
738 2D-S (Stereo) Probe: Design and Preliminary Tests of a New Airborne, High-Speed,
739 High-Resolution Particle Imaging Probe. *J. Atmos. Oceanic Technol.*, **23**, 1462–
740 1477, <https://doi.org/10.1175/JTECH1927.1>.

741 Liou, K.-N., and P. Yang, 2016: Light Scattering by Ice Crystals by Kuo-Nan Liou.
742 *Cambridge Core*, <https://doi.org/10.1017/CBO9781139030052>.

743 Lolli, S., E. J. Welton, and J. R. Campbell, 2013: Evaluating Light Rain Drop Size
744 Estimates from Multiwavelength Micropulse Lidar Network Profiling. *J. Atmos.*
745 *Oceanic Technol.*, **30**, 2798–2807, <https://doi.org/10.1175/JTECH-D-13-00062.1>.

746 Mason, J., W. Strapp, and P. Chow, 2006: The Ice Particle Threat to Engines in Flight.
747 *44th AIAA Aerospace Sciences Meeting and Exhibit*, 44th AIAA Aerospace Sciences
748 Meeting and Exhibit, Reno, Nevada, American Institute of Aeronautics and
749 Astronautics.

750 McFarquhar, G. M., and Coauthors, 2017: Processing of Ice Cloud In Situ Data Collected
751 by Bulk Water, Scattering, and Imaging Probes: Fundamentals, Uncertainties, and
752 Efforts toward Consistency. *Meteorological Monographs*, **58**, 11.1-11.33,
753 <https://doi.org/10.1175/AMSMONOGRAPHS-D-16-0007.1>.

754 Mishchenko, M. I., L. D. Travis, and D. W. Mackowski, 1996: T-matrix computations of
755 light scattering by nonspherical particles: A review. *Journal of Quantitative*
756 *Spectroscopy and Radiative Transfer*, **55**, 535–575, [https://doi.org/10.1016/0022-](https://doi.org/10.1016/0022-4073(96)00002-7)
757 [4073\(96\)00002-7](https://doi.org/10.1016/0022-4073(96)00002-7).

758 O’Shea, S. J., J. Crosier, J. Dorsey, W. Schledewitz, I. Crawford, S. Borrmann, R. Cotton,
759 and A. Bansemer, 2019: Revisiting particle sizing using greyscale optical array
760 probes: evaluation using laboratory experiments and synthetic data. *Atmospheric*
761 *Measurement Techniques*, **12**, 3067–3079, [https://doi.org/10.5194/amt-12-3067-](https://doi.org/10.5194/amt-12-3067-2019)
762 [2019](https://doi.org/10.5194/amt-12-3067-2019).

763 Ray, M., and K. Anderson, 2015: Analysis of Flight Test Results of the Optical Ice
764 Detector. *SAE Int. J. Aerosp.*, **8**, 1–8, <https://doi.org/10.4271/2015-01-2106>.

765 ———, M. Nesnidal, and D. Socha, 2009: Optical Detection of Airborne Ice Crystals and
766 Liquid Water Droplets. *1st AIAA Atmospheric and Space Environments Conference*,
767 American Institute of Aeronautics and Astronautics.

768 Rosenfeld, D., and W. L. Woodley, 2000: Deep convective clouds with sustained
769 supercooled liquid water down to -37.5 °C. *Nature*, **405**, 440–442,
770 <https://doi.org/10.1038/35013030>.

771 Schmidt, J. M., and Coauthors, 2019: Radar Detection of Individual Raindrops. *Bull.*
772 *Amer. Meteor. Soc.*, <https://doi.org/10.1175/BAMS-D-18-0130.1>.

773 Schön, R., and Coauthors, 2011: Particle Habit Imaging Using Incoherent Light: A First
774 Step toward a Novel Instrument for Cloud Microphysics. *J. Atmos. Oceanic*
775 *Technol.*, **28**, 493–512, <https://doi.org/10.1175/2011JTECHA1445.1>.

776 Shishko, V. A., A. V. Konoshonkin, N. V. Kustova, and D. N. Timofeev, 2020: Light
777 scattering by spherical particles for data interpretation of mobile lidars. *OE*, **59**,
778 083103, <https://doi.org/10.1117/1.OE.59.8.083103>.

779 Skofronick-Jackson, G., and Coauthors, 2014: Global Precipitation Measurement Cold
780 Season Precipitation Experiment (GCPEX): For Measurement’s Sake, Let It Snow.
781 *Bull. Amer. Meteor. Soc.*, **96**, 1719–1741, [https://doi.org/10.1175/BAMS-D-13-](https://doi.org/10.1175/BAMS-D-13-00262.1)
782 [00262.1](https://doi.org/10.1175/BAMS-D-13-00262.1).

783 Spanu, A., M. Dollner, J. Gasteiger, T. P. Bui, and B. Weinzierl, 2020: Flow-induced
784 errors in airborne in situ measurements of aerosols and clouds. *Atmospheric*
785 *Measurement Techniques*, **13**, 1963–1987, [https://doi.org/10.5194/amt-13-1963-](https://doi.org/10.5194/amt-13-1963-2020)
786 [2020](https://doi.org/10.5194/amt-13-1963-2020).

787 Wagner, S., 2020: Comparison of Backscatter Coefficients for Airborne Cloud Probes.
788 Masters Thesis, Dept. of Atmospheric Sciences, University of North Dakota, 64 pp.

789 —, Delene, D., 2020a: Analysis of Concurrent Backscatter Coefficients from In-situ
790 Cloud Probes and Airborne Lidar. University of North Dakota, accessed 05 May
791 2020, <https://commons.und.edu/data/15>

792 —, —, 2020b: OID Analysis (Version 1), Zenodo, doi:10.5281/zenodo.3740798.

793 Warren, S. G., and R. E. Brandt, 2008: Optical constants of ice from the ultraviolet to the
794 microwave: A revised compilation. *Journal of Geophysical Research: Atmospheres*,
795 **113**, <https://doi.org/10.1029/2007JD009744>.

796 Wesely, M. L., 1976: The Combined Effect of Temperature and Humidity Fluctuations on
797 Refractive Index. *J. Appl. Meteor.*, **15**, 43–49, [https://doi.org/10.1175/1520-](https://doi.org/10.1175/1520-0450(1976)015<0043:TCEOTA>2.0.CO;2)
798 [0450\(1976\)015<0043:TCEOTA>2.0.CO;2](https://doi.org/10.1175/1520-0450(1976)015<0043:TCEOTA>2.0.CO;2).

799 Wu, W., and G. M. McFarquhar, 2016: On the Impacts of Different Definitions of
800 Maximum Dimension for Nonspherical Particles Recorded by 2D Imaging Probes. *J.*
801 *Atmos. Oceanic Technol.*, **33**, 1057–1072, [https://doi.org/10.1175/JTECH-D-15-](https://doi.org/10.1175/JTECH-D-15-0177.1)
802 [0177.1](https://doi.org/10.1175/JTECH-D-15-0177.1).

803 Yang, P., and K. N. Liou, 1995: Light scattering by hexagonal ice crystals: comparison of
804 finite-difference time domain and geometric optics models. *J. Opt. Soc. Am. A*,
805 *JOSAA*, **12**, 162–176, <https://doi.org/10.1364/JOSAA.12.000162>.

806 ———, H. Wei, G. W. Kattawar, Y. X. Hu, D. M. Winker, C. A. Hostetler, and B. A. Baum,
807 2003: Sensitivity of the backscattering Mueller matrix to particle shape and
808 thermodynamic phase. *Appl. Opt.*, *AO*, **42**, 4389–4395,
809 <https://doi.org/10.1364/AO.42.004389>.

810 ———, ———, H.-L. Huang, B. A. Baum, Y. X. Hu, G. W. Kattawar, M. I. Mishchenko, and
811 Q. Fu, 2005: Scattering and absorption property database for nonspherical ice
812 particles in the near- through far-infrared spectral region. *Appl. Opt.*, *AO*, **44**, 5512–
813 5523, <https://doi.org/10.1364/AO.44.005512>.

- 814 Zhang, F., J. Pyle, and G. R. North, 2015: *Encyclopedia of Atmospheric Sciences*.
815 Academic Press.
- 816 Zhou, C., and P. Yang, 2015: Backscattering peak of ice cloud particles. *Opt. Express*,
817 *OE*, **23**, 11995–12003, <https://doi.org/10.1364/OE.23.011995>.

818 **Tables**

819 TABLE 1. Table listing parameters for the particle size distribution created by combining
 820 Two-Dimensional Stereo (2D-S) and High-Volume Precipitation Spectrometer Version 3
 821 (HVPS3) probe measurements. The Number Column lists the combined spectrum
 822 channel number, the Probe Column indicates which probe made the measurements, and
 823 Bin Columns gives the original probe’s channel number and total channels. The Size
 824 Range Column gives the lower and upper size of particles within the channel. The Size
 825 Parameter Column gives the scattering size parameter (3) range for the lower and upper
 826 particle sizes and a wavelength of 905 nm. The Water Column lists backscatter efficiency
 827 for water particles, and the Ice Column lists backscatter efficiency for ice particles. The Q
 828 Ratio Column gives ratio of backscatter efficiency of water to the backscatter efficiency
 829 of ice. The MiePlot software package is used to calculate average efficiencies using
 830 particles diameters that span the combined spectrum width (black circles in Fig. 3).

Number	Probe	Bin	Size Range	Size Parameter	Q(Water)	Q(Ice)	Q Ratio
1	2D-S	1 / 29	5 – 15 μm	17 – 52	0.1184	0.1276	0.9276
2	2D-S	2 / 29	15 – 25 μm	52 – 87	0.1128	0.1204	0.9369
3	2D-S	3 / 29	25 – 35 μm	87 – 122	0.1137	0.1412	0.8052
4	2D-S	4 / 29	35 – 45 μm	122 – 156	0.1142	0.1463	0.7806
5	2D-S	5 / 29	45 – 55 μm	156 – 191	0.1183	0.1456	0.8125
6	2D-S	6 / 29	55 – 65 μm	191 – 226	0.1172	0.1398	0.8383
7	2D-S	7 / 29	65 – 75 μm	226 – 260	0.1280	0.1355	0.9446
8	2D-S	8 / 29	75 – 85 μm	260 – 295	0.1269	0.1328	0.9556
9	2D-S	9 / 29	85 – 95 μm	295 – 330	0.1401	0.1247	1.1235
10	2D-S	10 / 29	95 – 105 μm	330 – 364	0.1399	0.1184	1.1816
11	2D-S	11 / 29	105 – 125 μm	364 – 434	0.1546	0.1137	1.3597
12	2D-S	12 / 29	125 – 145 μm	434 – 503	0.1634	0.1032	1.5833
13	2D-S	13 / 29	145 – 175 μm	503 – 607	0.1809	0.0932	1.9410
14	2D-S	14 / 29	175 – 225 μm	607 – 781	0.2070	0.0786	2.6336
15	2D-S	15 / 29	225 – 275 μm	781 – 955	0.2277	0.0663	3.4344

16	2D-S	16 / 29	275 – 325 µm	955 – 1128	0.2547	0.0590	4.3169
17	2D-S	17 / 29	325 – 400 µm	1128 – 1389	0.2728	0.0508	5.3701
18	2D-S	18 / 29	400 – 475 µm	1389 – 1649	0.2966	0.0486	6.1029
19	2D-S	19 / 29	475 – 550 µm	1649 – 1909	0.3182	0.0424	7.5047
20	2D-S	20 / 29	550 – 625 µm	1909 – 2170	0.3434	0.0404	8.5000
21	2D-S	21 / 29	625 – 700 µm	2170 – 2430	0.3581	0.0369	9.7046
22	2D-S	22 / 29	700 – 800 µm	2430 – 2777	0.3860	0.0321	12.025
23	2D-S	23 / 29	800 – 900 µm	2777 – 3124	0.3988	0.0314	12.701
24	2D-S	24 / 29	900 – 1,000 µm	3124 – 3471	0.4157	0.0276	15.062
25	HVPS3	5 / 28	1000 – 1200 µm	3471 – 4166	0.4390	0.0270	16.259
26	HVPS3	6 / 28	1200 – 1400 µm	4166 – 4860	0.4793	0.0238	20.139
27	HVPS3	7 / 28	1400 – 1600 µm	4860 – 5554	0.5139	0.0238	21.592
28	HVPS3	8 / 28	1600 – 1800 µm	5554 – 6248	0.5532	0.0215	25.730
29	HVPS3	9 / 28	1800 – 2200 µm	6248 – 7637	0.5831	0.0190	30.690
30	HVPS3	10 / 28	2200 – 2600 µm	7637 – 9025	0.6419	0.0171	37.538
31	HVPS3	11 / 28	2600 – 3000 µm	9025 – 10 414	0.6952	0.0154	45.143
32	HVPS3	12 / 28	3000 – 3400 µm	10 414 – 11 803	0.7173	0.0147	48.796
33	HVPS3	13 / 28	3400 – 3800 µm	11 803 – 13 191	0.7722	0.0132	58.500
34	HVPS3	14 / 28	3800 – 4200 µm	13 191 – 14 580	0.8018	0.0130	61.677
35	HVPS3	15 / 28	4200 – 4600 µm	14 580 – 15 968	0.8290	0.0121	68.512
36	HVPS3	16 / 28	4600 – 5000 µm	15 968 – 17 357	0.8433	0.0122	69.123
37	HVPS3	17 / 28	5000 – 6000 µm	17 357 – 20 828	0.8479	0.0118	71.856
38	HVPS3	18 / 28	6000 – 7000 µm	20 828 – 24 300	0.8409	0.0116	72.491
39	HVPS3	19 / 28	7000 – 8000 µm	24 300 – 27 771	0.8017	0.0111	72.225
40	HVPS3	20 / 28	8000 – 9000 µm	27 771 – 31 242	0.7330	0.0110	66.636
41	HVPS3	21 / 28	9000 – 10 000 µm	31 242 – 34 714	0.6373	0.0104	61.279
42	HVPS3	22 / 28	10 000 – 12 000 µm	34 714 – 41 656	0.4916	0.0101	48.673
43	HVPS3	23 / 28	12 000 – 14 000 µm	41 656 – 48 599	0.3467	0.0100	34.670
44	HVPS3	24 / 28	14 000 – 16 000 µm	48 599 – 55 542	0.2962	0.0104	28.481
45	HVPS3	25 / 28	16 000 – 18 000 µm	55 542 – 62 485	0.3878	0.0098	39.571
46	HVPS3	26 / 28	18 000 – 20 000 µm	62 485 – 69 427	0.5822	0.0103	56.524
47	HVPS3	27 / 28	20 000 – 25 000 µm	69 427 – 86 784	0.9381	0.0098	95.725
48	HVPS3	28 / 28	25 000 – 30 000 µm	86 784 – 104 141	0.9826	0.0092	106.80

831 TABLE 2. Table listing details of the 60 s segments for the Florida, CAPE2015 case
832 studies. Numbers in parentheses in the Flight Row indicate the first (1) or second (2)
833 flight conducted on the given day. The Time Row gives the segment start and end times
834 in seconds from midnight (sfm) UTC. The Altitude Row gives the average and standard
835 deviation of the Citation Aircraft’s GPS altitude. The Temp Row gives the average and
836 standard deviation of the aircraft measured air temperature. The Latitude Row gives
837 minimum and maximum latitudes. The Longitude Row gives minimum and maximum
838 longitudes. The Cloud Base and Cloud Top rows give cloud base and top altitudes,
839 respectively, derived from the National Weather Service Melbourne radar. “Not
840 Available” indicates insufficient radar reflectivity to detect the cloud. The TWC Row
841 gives the average and standard deviation of the total water content (TWC) measured by
842 the Nevzorov probe.

Case	+7°C	+4°C	-33°C	-46°C
Flight	02 August 2015	01 August 2015 (1)	31 July 2015	01 August 2015 (2)
Time	69 510 – 69 570 sfm	57 850- 57 910 sfm	71 710 – 71 770 sfm	72 700 – 72 760 sfm
Altitude	3043 m ± 17.2 m	3440 m ± 3.3 m	9479 m ± 3.8 m	10 971 m ± 6.8 m
Temp	6.7°C ± 0.42°C	4.3°C ± 0.11°C	-33.0°C ± 0.12°C	-45.9°C ± 0.27°C
Latitude	28.446° - 28.497°N	28.725° - 28.761°N	28.326° - 28.402°N	28.408° - 28.480°N
Longitude	80.4916° - 80.4859°W	80.5915° - 80.5577°W	80.445° - 80.4373°W	80.714° - 80.686°W
Cloud Base	Not Available	Not Available	1000 m	1000 m
Cloud Top	Not Available	Not Available	11 000 m	15 000 m
TWC	1.2 g m ⁻³ ± 0.47 g m ⁻³	0.5 g m ⁻³ ± 0.08 g m ⁻³	0.1 g m ⁻³ ± 0.05 g m ⁻³	0.1 g m ⁻³ ± 0.02 g m ⁻³

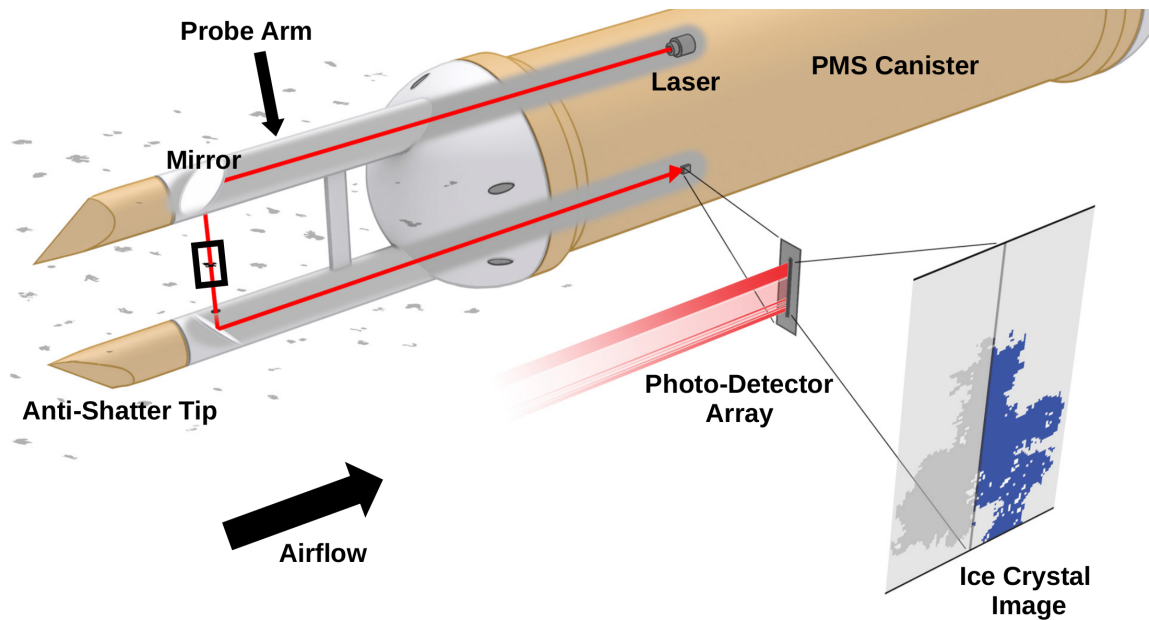


FIG. 1. Illustration showing the side view of a two-dimensional optical array probe in a particle measurement system (PMS) canister. Images are obtained as particles pass through the laser beam (red line) when the aircraft's speed creates airflow past the probe. The laser beam is directed between the probe arms using two 90 degree mirrors. Particles passing through the laser beam block light causing reduced illumination on the photodiode array. Images are produced when at least one array element is reduced in intensity by a set amount (*e.g.* 50%). The depth of field (the location where the particle must cross the beam to be clearly imaged) is indicated with a black rectangle. The sampling frequency of the photo-detector array is adjusted using the measured true air speed so images (example given in lower right) have symmetric pixel elements. Heated, anti-shattering tips prevent ice accretion and reduce the number of shattered particles that enter the sample volume.

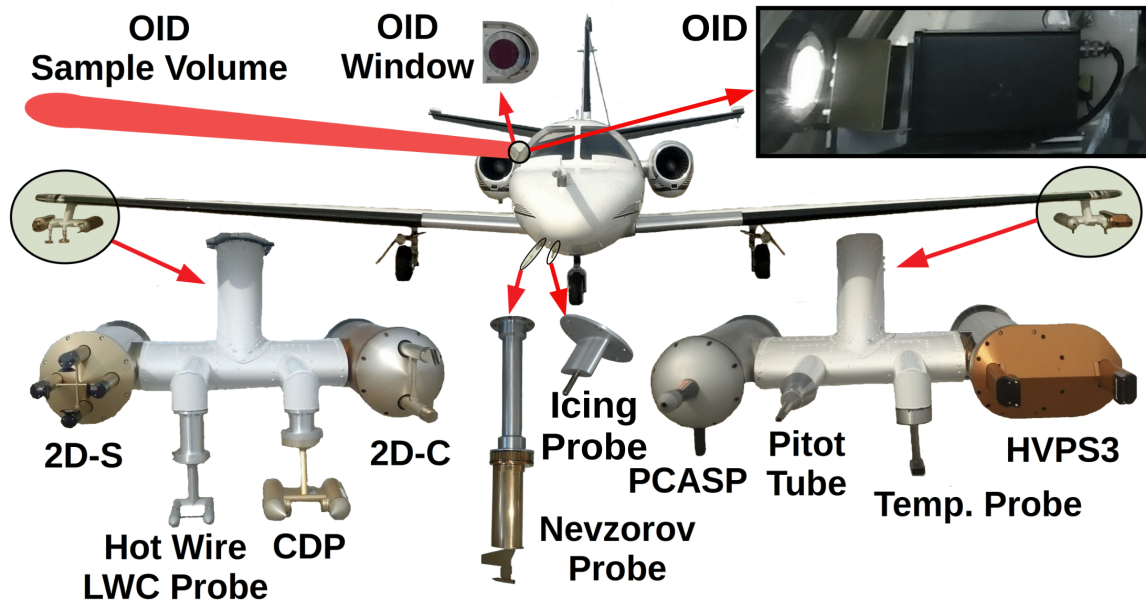


FIG. 2. Image showing the North Dakota Citation Research Aircraft with an enlarged view of the wing-tip pylons, the Nevzorov probe and the Rosemount Icing Probe as mounted for the 2015 field project over Cape Canaveral, Florida (CAPE2015). OID Window (upper center) is the viewing port through the pressurized cabin for the Optical Ice Detector (OID). The OID is angled slightly (10-15 degrees) forward of the wing so the sampling region (OID Sample Volume) is in front of and above the right wing. An image of the OID in the Citation fuselage is shown in the upper right. The Cloud Droplet Probe (CDP) measures particles from two to 50 μm (30 channels) using forward light scattering. The Two-Dimensional Stereo (2D-S) probe measures particles using shadowed diodes (two (one horizontal and one vertical) 128 element arrays) of 10 μm . The High-Volume Precipitation Spectrometer Version 3 (HVPS3) measures particles using shadow diodes (128 element array) of 150 μm . The Two Dimensional Cloud probe (2D-C) is an older probe that also measures particles using shadowed diodes (32 element array) of 30

μm . The Rosemount Icing Probe detects super-cooled liquid water using a vibrating metal rod. The Nevzorov probe is a hot-wire probe that measures liquid and total water content. Subtracting the liquid water content from the total water content determines the ice water content. The King Hot Wire Liquid Water Content (LWC) Probe is an older probe that only measures liquid water content. The Passive Cavity Aerosol Spectrometer Probe (PCASP) model measures aerosols from 0.1 to 3.0 μm . The Rosemount temperature probe (Temp. Probe) measures ambient air temperature, and the pitot tube measures air speed using a differential pressure transducer connected to a static and a forward facing port.

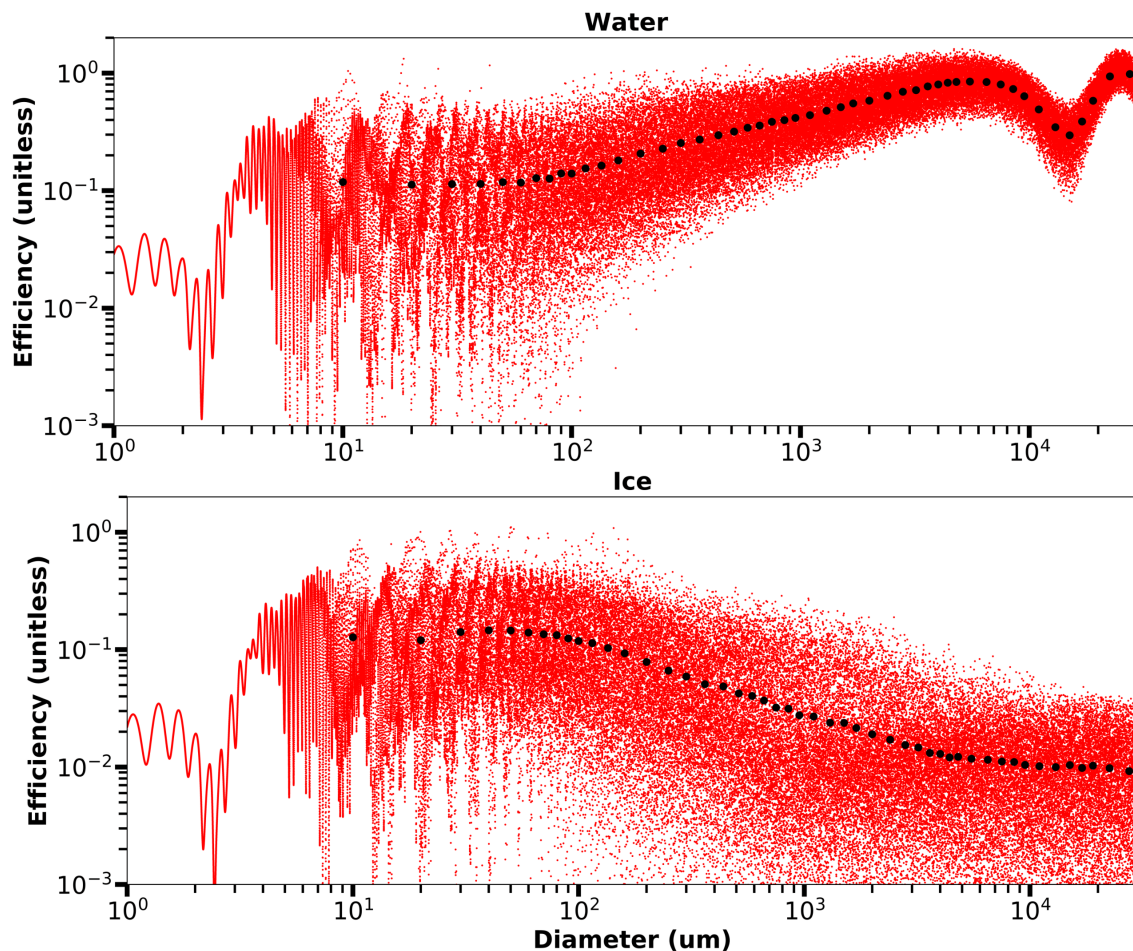


FIG. 3. Plots showing backscatter efficiencies using Mie theory for spherical water (top) and ice (bottom) particles. The MiePlot software package (Laven 2018) is used to calculate efficiencies for 100 000 particle diameters distributed log-normally between 1 μm and 30 mm (red dots). Intervals range from 0.0001 μm between the smallest diameters to 3 μm between the largest diameters. Black circles are average efficiencies over the combined spectrum channel widths (see Table 1 for numerical values). A refractive index of $1.3263 + 5.6 \times 10^{-7}j$ is used for water (Kedenburg *et al.* 2012) and $1.3031 + 5.6 \times 10^{-7}j$ for ice (Warren and Brandt 2008). Scattering is for an air medium at 20°C and incident light of 905 nm.

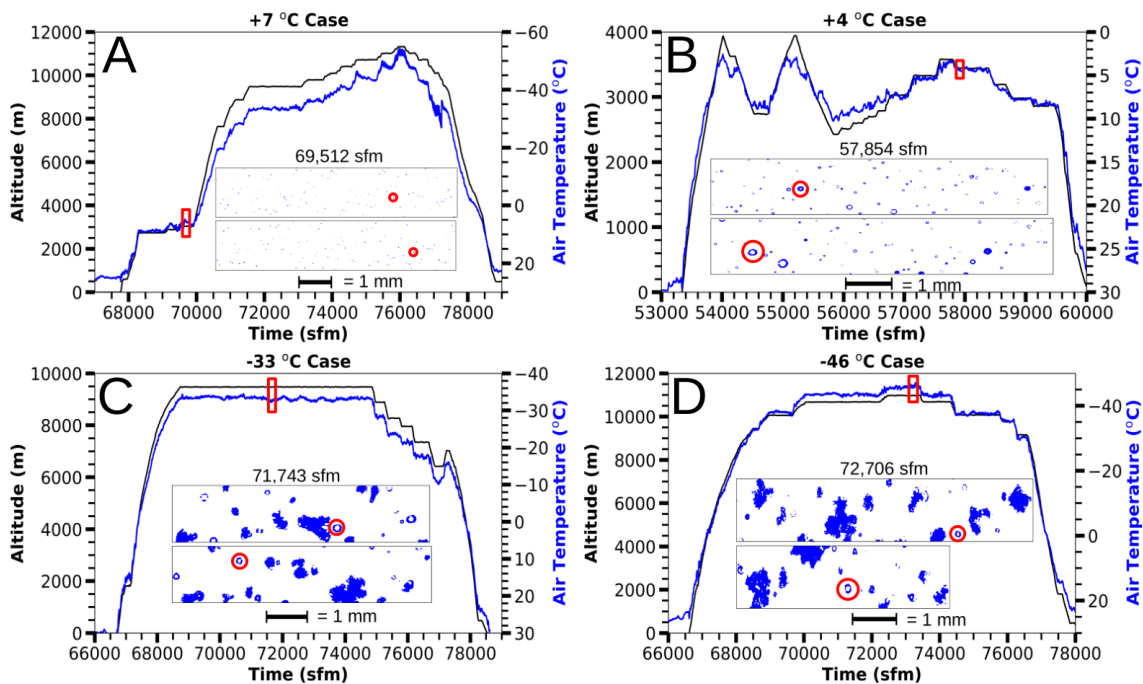


FIG. 4. Plots showing time series in seconds from midnight (sfm) Coordinated Universal Time (UTC) of altitude (black) and air temperature (blue) for four analyzed flights. The red rectangles enclose the 60 s case study segments associated with each flight. Details for each segment are given in Table 2. Center panels contain representative 2D-S images from within the analyzed cases. Red circles within the 2D-S images show examples of particles with Poisson spots that are discussed in the text. The upper, red circle marked particle for the -33°C case is approximately 180 μm in diameter.

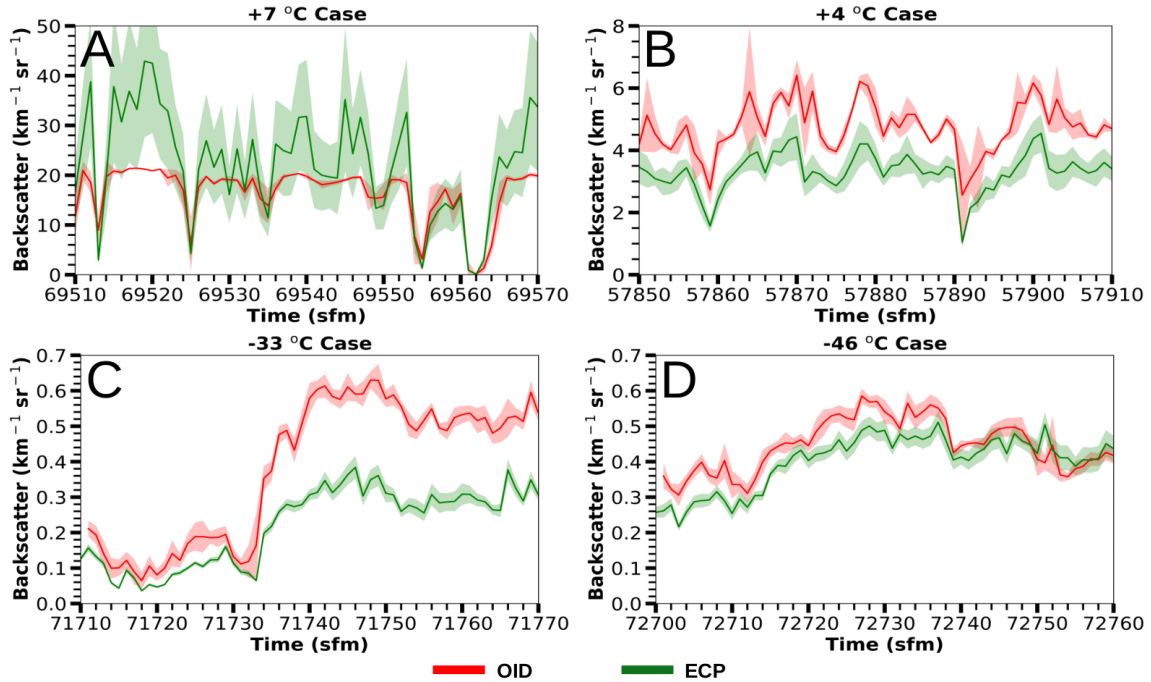


FIG. 5. Plots showing 1 Hz time series in seconds from midnight (sfm) Coordinated Universal Time (UTC) of backscatter coefficients with a shadowed range for the four case study segments (Table 2). Note the differing backscatter coefficient scales for the warm cloud cases. The external cloud probes (ECP) shadowed range is the measurement uncertainty determined from (5), and represents one standard deviation. The Optical Ice Detector (OID) shadowed range is one standard deviation computed from averaging the OID data rate from 5 Hz to 1 Hz.

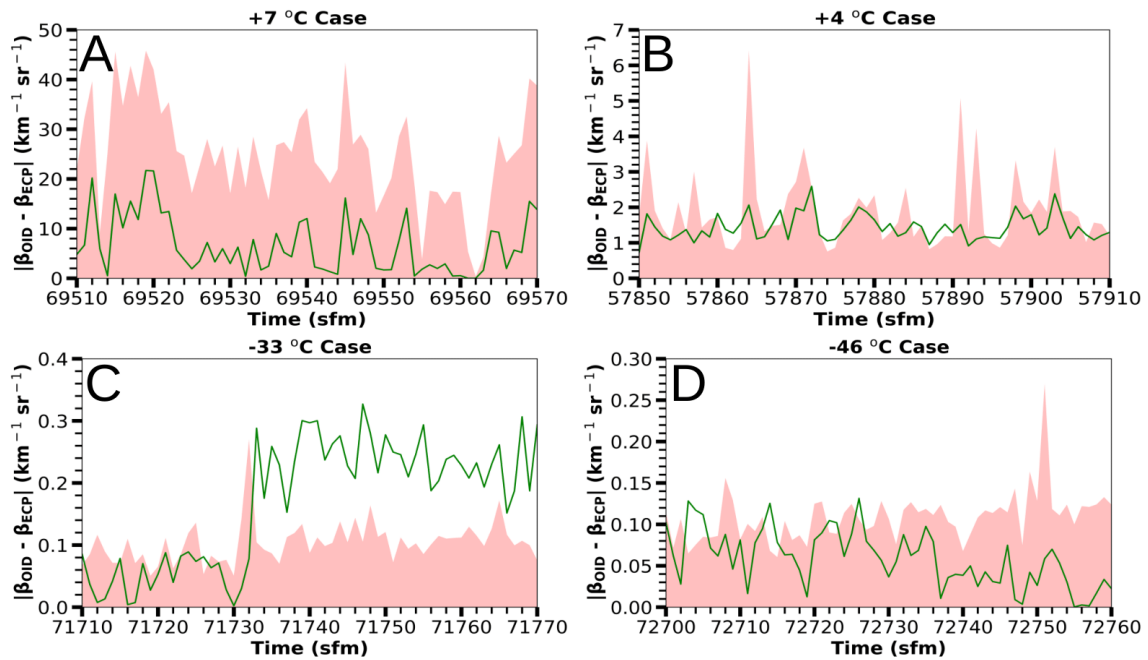


FIG. 6. Plots showing 1 Hz time series in seconds from midnight (sfm) Coordinated Universal Time (UTC) of the absolute difference between the Optical Ice Detector (OID) and external cloud probes (ECP) backscatter coefficients for the four case study segments (Table 2). The green line is the absolute difference of the OID and ECP backscatter coefficients. The shadowed region top represents three standard deviations of OID and ECP backscatter coefficients, determined using (7).

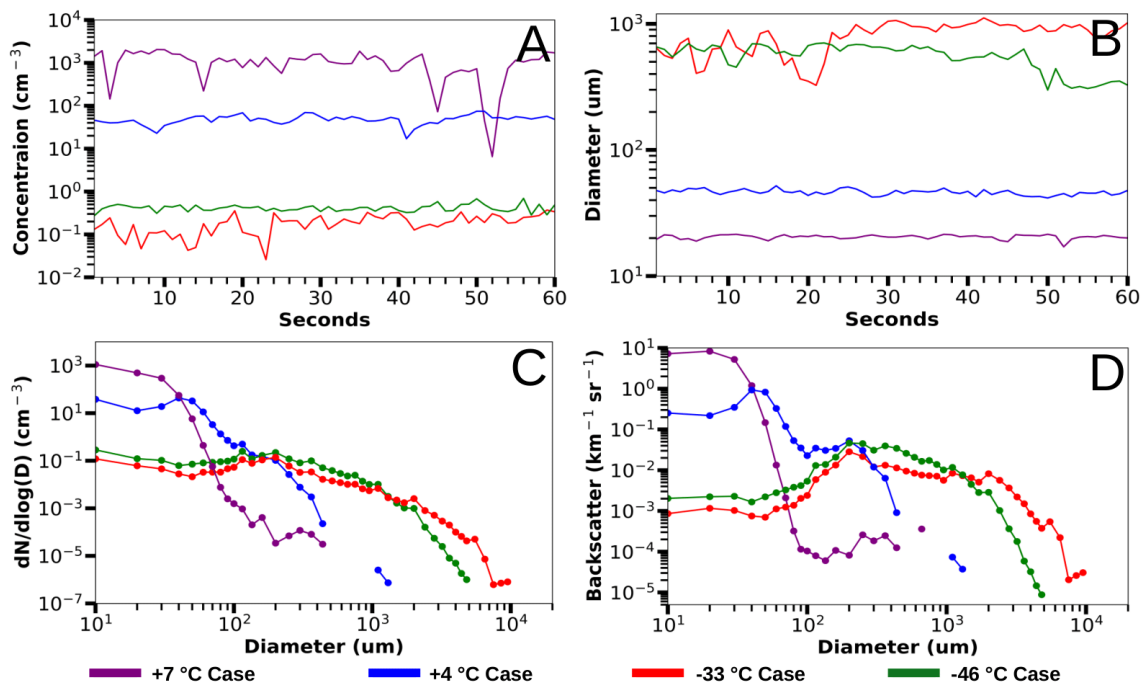


FIG. 7. Plots showing measurements within the 60 s segments of four analyzed cases (Table 2). The upper left plot (A) is total number concentration measured by the external cloud probes (ECP), specifically the Two-Dimensional Stereo (2D-S) and High-Volume Precipitation Spectrometer Version Three (HVPS3) probes (Table 1). The upper right plot (B) is mean particle diameter measured by the ECP. The lower left plot (C) is a log-log plot of number density function vs. diameter measured by the ECP. The lower right plot (D) shows ECP backscatter coefficient versus the particle diameter. The y-axis of plot D is not normalized by size channel width.

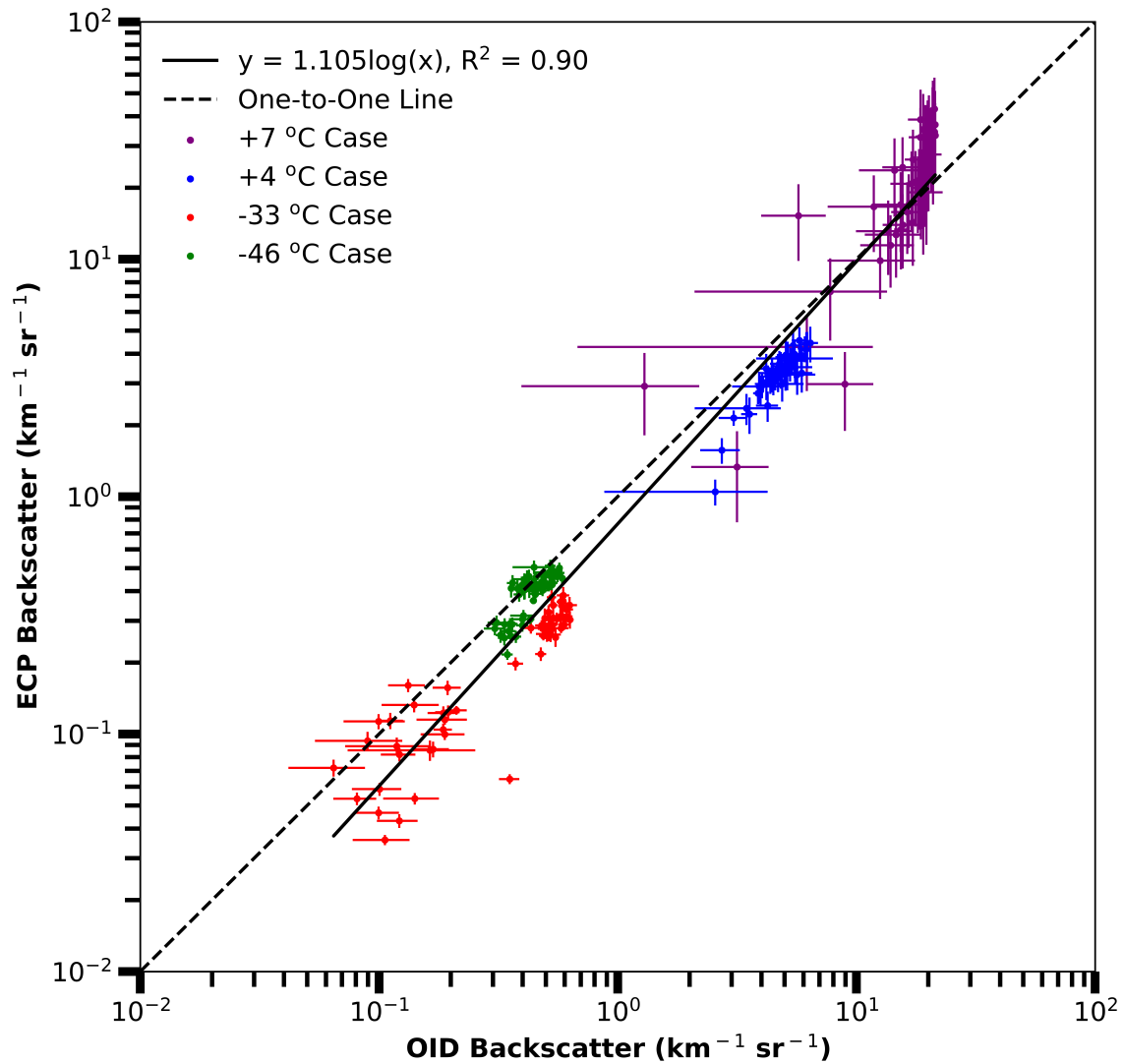


FIG. 8. The Optical Ice Detector (OID) versus external cloud probes (ECP) backscatter coefficients for four analyzed cases (Table 2). Each dot is colored by case (see legend) and represents 1 s of data (Fig. 5) with bars indicating uncertainty. The least square fit is given by the black line (see equation in legend). The dashed line is a one-to-one correspondence for the ECP and OID data.

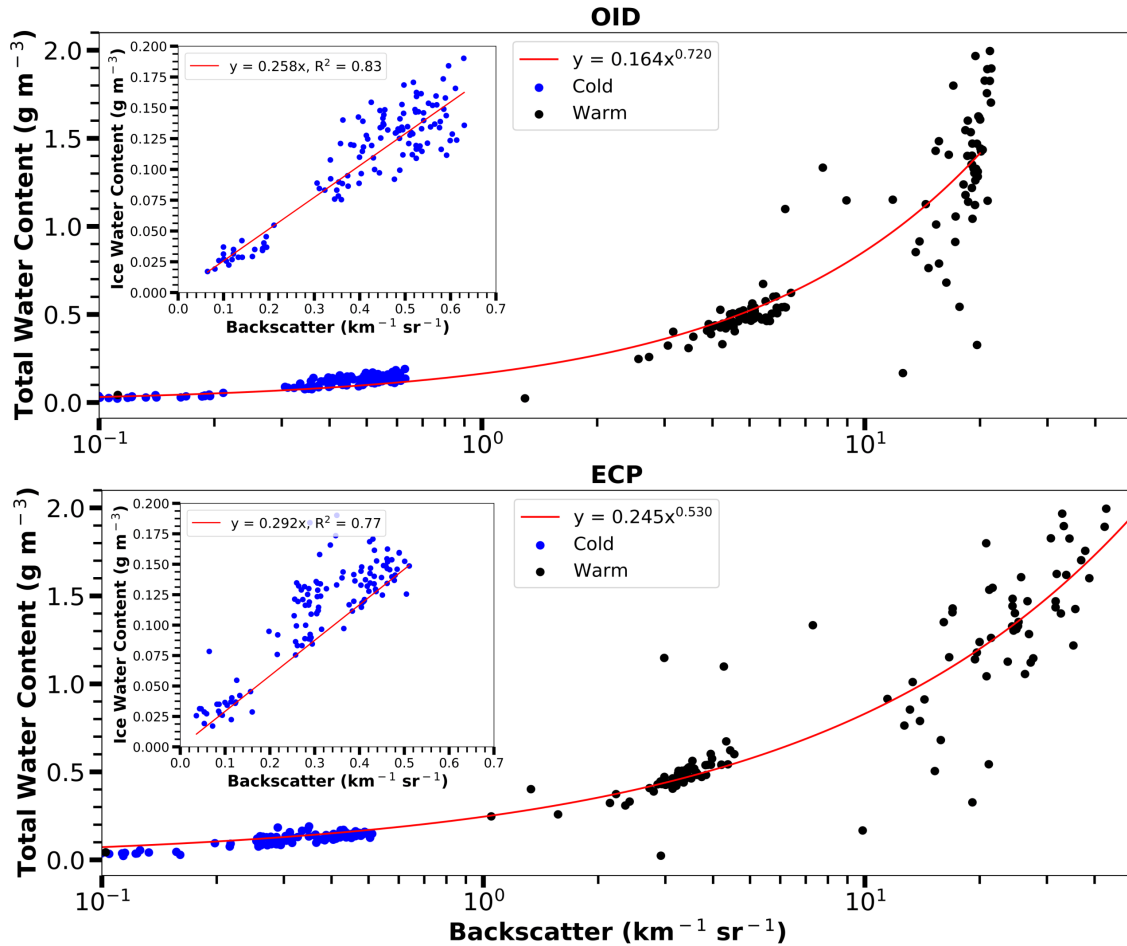


FIG. 9. Plots showing Nevzorov probe total water content versus Optical Ice Detector (OID) backscatter coefficients (top) and external cloud probes (ECP) backscatter coefficients (bottom) with a logarithmic x-axis. Backscatter coefficients are separated by warm (+7°C and +4°C) cases and cold (-33°C and -46°C) cases (Table 2). Insets in the top-left corners show further detail of Nevzorov probe total water content versus respective backscatter coefficients for the -33°C and -46°C cases. Each dot represents 1 s of Nevzorov, OID, and ECP data.

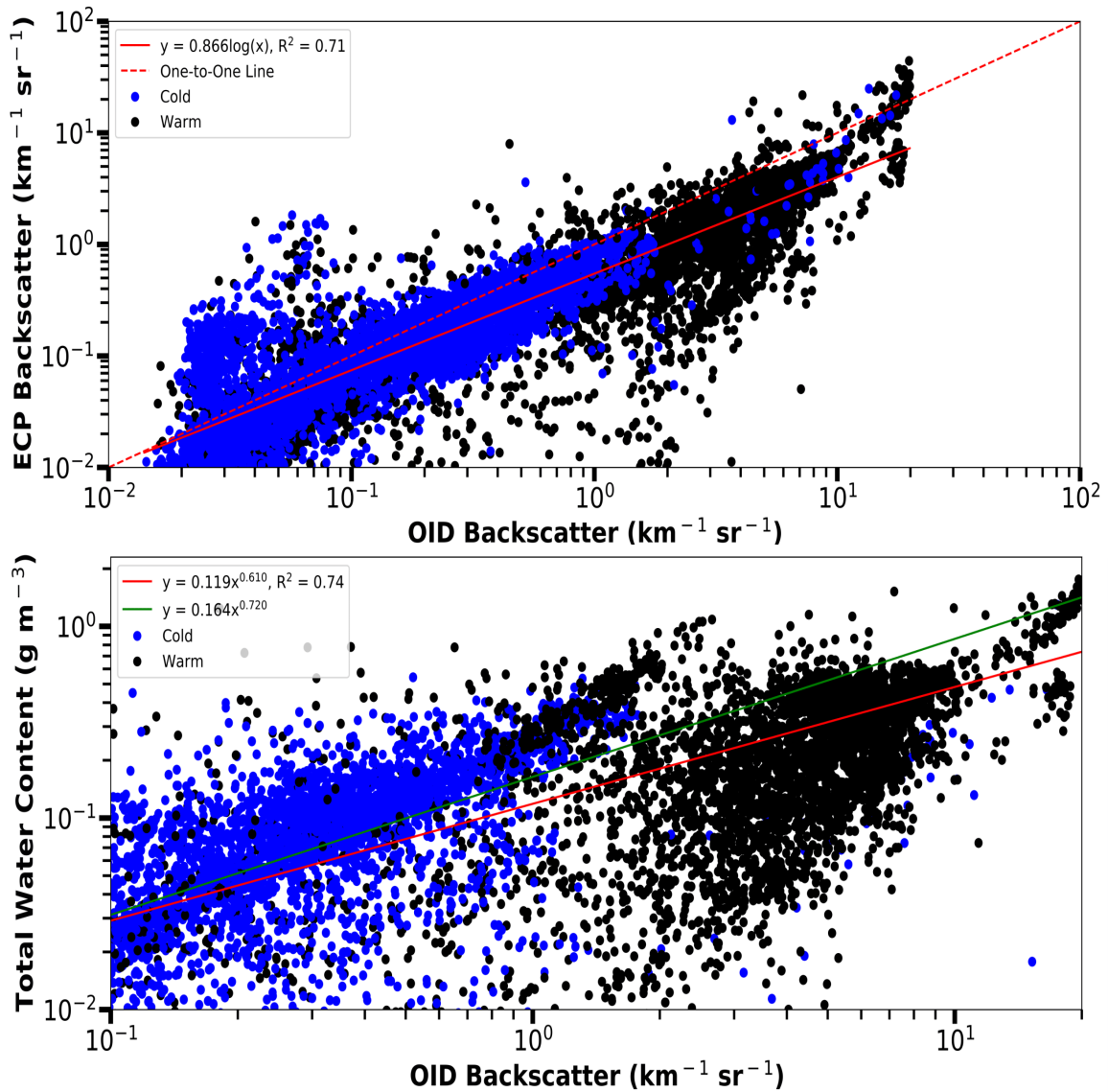


FIG. 10. The external cloud probes (ECP) backscatter coefficients versus Optical Ice Detector (OID) backscatter coefficients (top) and Nevzorov probe total water contents versus OID backscatter coefficients (bottom) for all times within the four flights (Table 2) that contain the four temperature cases. The 1 Hz data is grouped by cold (blue) and warm (black) environments. Data are excluded when temperatures are between 0°C and -20°C . Liquid scattering efficiencies are used for temperatures greater than 0°C and ice

scattering efficiencies used for temperatures below -20°C . OID data has a $20\text{ km}^{-1}\text{sr}^{-1}$ limit to avoid times where observations are above the OID's detection limit. The lower plot's green line indicates the fit equation in Fig. 9.

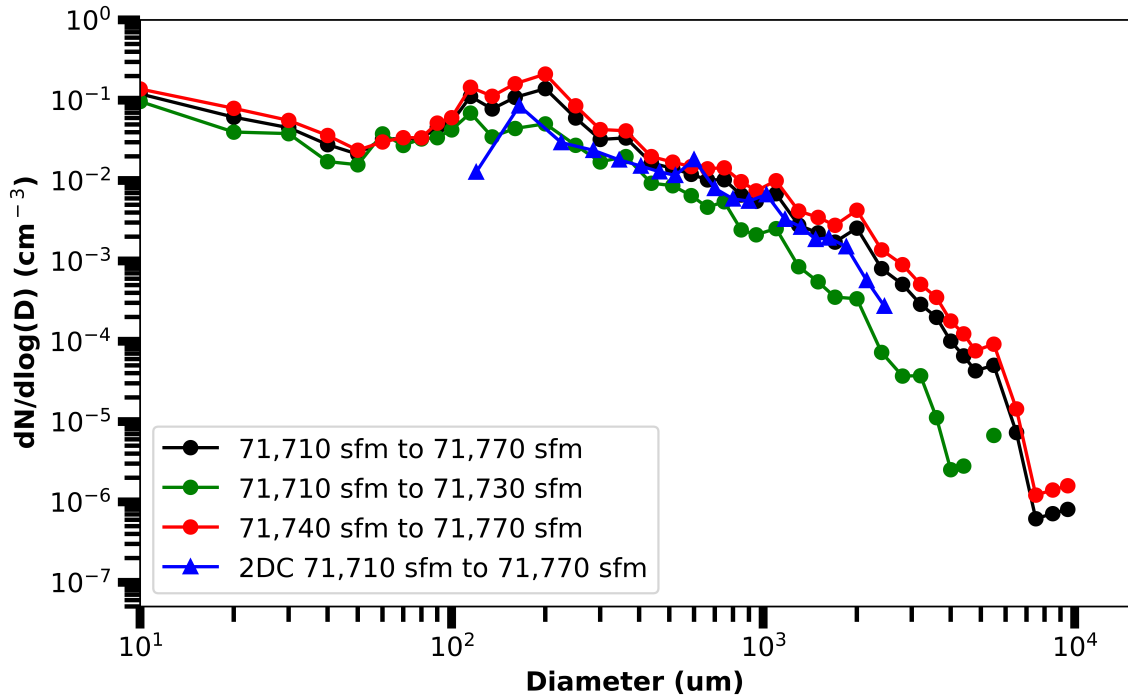


FIG. 11. The size spectrum normalized by bin width measured by the external cloud probes (ECP) for the -33°C case (Table 2). The spectrum of the entire 60 s case (black) has been separated according to times of more (green) and less (red) agreement between ECP and Optical Ice Detector (OID) backscatter coefficients. Also given is the 2D-C spectrum obtained using the full particle reconstruction processing method.

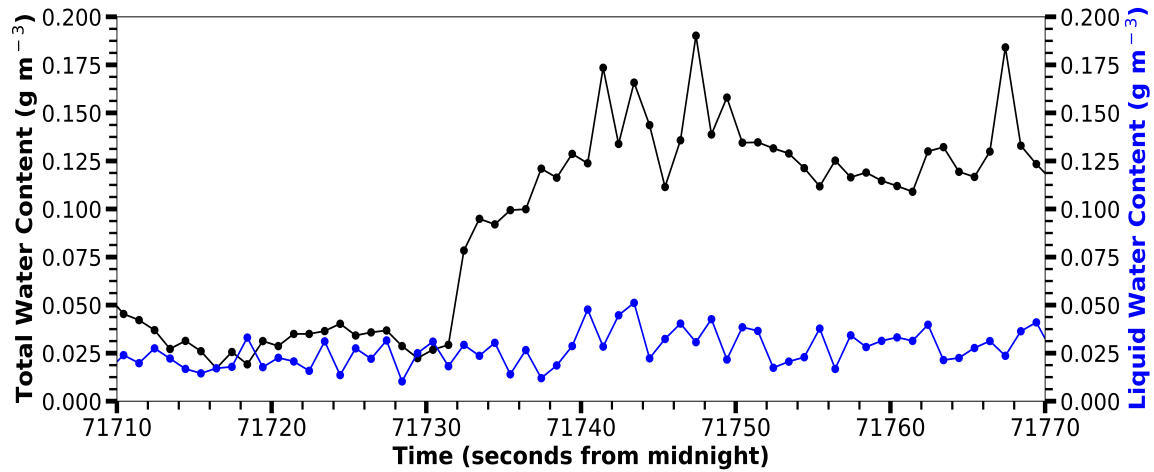


FIG. 12. Nevzorov probe measured total water content (black) and liquid water content (blue) for the -33°C case (Table 2). Each dot represents 1 s of Nevzorov data. The average liquid water content is $0.022 \text{ g m}^{-3} \pm 0.009 \text{ g m}^{-3}$ and the average total water content is $0.032 \text{ g m}^{-3} \pm 0.008 \text{ g m}^{-3}$ during times of Optical Ice Detector (OID) and external cloud probe (ECP) backscatter coefficient agreement (71 710 sfm to 71 730 sfm). The average liquid water content is $0.027 \text{ g m}^{-3} \pm 0.009 \text{ g m}^{-3}$ and the average total water content is $0.092 \text{ g m}^{-3} \pm 0.05 \text{ g m}^{-3}$ during times of OID and ECP backscatter coefficient disagreement (71 740 sfm to 71 770 sfm).